The Effect of Grain Size on Porewater Radiolysis

Joel DeWitt[1], Sean McMahon[2], and John Parnell[3]

[1]East Carolina University
[2]University of Edinburgh
[3]University of Aberdeen

November 23, 2022

Abstract

The radiolysis of porewaters by uranium, thorium, and potassium in mineral grains is a recognised source of molecular hydrogen in rock- and sediment-hosted fluids. This radiolytic hydrogen is of geomicrobiological interest as a potential energy source (electron donor) for microbial metabolism, especially in energy-limited settings such as the marine deep biosphere or the subsurface of Mars. Previous efforts to predict the production of radiolytic hydrogen from columns of rock and sediment have tended to rely upon analytic models that cannot account for the attenuation of mineral radiation by grains larger than ˜30 microns. To address this, we have developed a Monte Carlo method to simulate the physics of mineral radiation and evaluate the production of H_2 as a function of mineral grain size and radioisotope composition. The results confirm that grain size is a major control on radiolytic H_2 yield. For example, using the standard geological classification of grain sizes, we find that clay can produce up to an order of magnitude more H_2 per unit time than sand. The magnitude of this effect is illustrated using compositional data from real geological units in order to demonstrate the dependence of radiolytic hydrogen flux on natural radionuclide concentration and bulk porosity.

Posted on 23 Nov 2022 — CC-BY-NC-ND 4 — https://doi.org/10.1002/essoar.10508053.1 — This a preprint and has not been peer reviewed. Data may be preliminary.

The Effect of Grain Size on Porewater Radiolysis

J. DeWitt[1], S. McMahon[2,3], and J. Parnell[4]

[1] Department of Physics, East Carolina University, Howell Science Complex, 10th Street, Greenville NC 27858, US

[2] School of Physics and Astronomy, University of Edinburgh, James Clerk Maxwell Building, Peter Guthrie Tait Road, Edinburgh EH9 3FD, UK

[3] School of Geosciences, University of Edinburgh, Grant Institute, Edinburgh EH9 3FE, UK

[4] School of Geosciences, University of Aberdeen, Meston Building, King's College, Aberdeen AB24 3UE

Corresponding authors: Joel DeWitt (dewittjo@ecu.edu), Sean McMahon (sean.mcmahon@ed.ac.uk)

Key Points:

- Porewater radiolysis in rocks and minerals yields molecular hydrogen (H_2), an energy source for microbial life on Earth and perhaps Mars.
- Our Monte Carlo simulations of mineral radiation reveal how grain size controls H_2 yield for a give radioisotope composition and porosity.
- For some realistic scenarios, clay can produce up to an order of magnitude more H_2 per unit time than sand.

Abstract

The radiolysis of porewaters by uranium, thorium, and potassium in mineral grains is a recognised source of molecular hydrogen in rock- and sediment-hosted fluids. This radiolytic hydrogen is of geomicrobiological interest as a potential energy source (electron donor) for microbial metabolism, especially in energy-limited settings such as the marine deep biosphere or the subsurface of Mars. Previous efforts to predict the production of radiolytic hydrogen from columns of rock and sediment have tended to rely upon analytic models that cannot account for the attenuation of mineral radiation by grains larger than ~30 microns. To address this, we have developed a Monte Carlo method to simulate the physics of mineral radiation and evaluate the production of H_2 as a function of mineral grain size and radioisotope composition. The results confirm that grain size is a major control on radiolytic H_2 yield. For example, using the standard geological classification of grain sizes, we find that clay can produce up to an order of magnitude more H_2 per unit time than sand. The magnitude of this effect is illustrated using compositional data from real geological units in order to demonstrate the dependence of radiolytic hydrogen flux on natural radionuclide concentration and bulk porosity.

1 Introduction

The oxidation of molecular hydrogen (hydrogenotrophy) provides energy for microbial growth in a wide variety of environments and may have sustained Earth's earliest metabolising organisms (e.g., Kral et al., 1998; Schulte et al., 2006; Sleep et al., 2011; Lane and Martin, 2012; Preiner et al., 2020). In subsurface habitats, naturally occurring H_2 serves as an electron donor for methanogens, acetogens, sulfate-reducers and other anaerobic microorganisms forming part of the "deep biosphere". Analogous habitats might potentially support similar metabolisms in the deep subsurface of Mars and other planets and moons (Stevens and McKinley, 1995; Chapelle et al., 2002; Nixon et al., 2013). Although there is no direct evidence for life on these worlds as yet, methane has been detected repeatedly in the Martian atmosphere (most recently by the Curiosity rover and Mars Express Orbiter; Webster et al., 2015; Giuranna et al., 2019), and molecular hydrogen is also present in aqueous plumes venting from the subsurface ocean of Saturn's moon Enceladus (Waite et al., 2017). Hypothetically, life on these worlds might be supplied with molecular hydrogen from several natural sources also known to be active on the Earth, including organic fermentation, reactions between water and silicate minerals (known as "serpentinization"; McCollom, 1999), diffusion from crystallographic defects (Freund et al., 2002), and the reduction of water during "mechanoradical" processes driven by frictional grinding on fault planes (Hirose et al., 2011; McMahon et al., 2016). Independently of these sources, H_2 is produced by extremely rapid interactions between protons, electrons and radical species released from water molecules under alpha, beta and gamma irradiation issuing from radioactive elements in minerals (^{235}U, ^{238}U, ^{232}Th, ^{40}K and their respective short-lived radiogenic daughters). Radiolysis is independent of temperature, and can generate H_2 from both porewater (including ice) and crystallographic water in hydrated minerals (Blair et al., 2007; Smetannikov, 2011). Water radiolysis also produces reactive oxygen species capable of oxidizing minerals to form electron acceptors such as SO_4^{2-}; radiolysis can thus support microbial life at both ends of the electron transport chain (Lefticariu et al., 2010).

Several studies have attempted to model the radiolytic hydrogen (H_2) flux from rocks and sediments beneath the seafloor and land surface under different conditions, including conditions that represent different planetary bodies. Lin et al. (2005) and Blair et al. (2007) considered crystalline continental rocks and marine shelf sediments, respectively, focusing on water-saturated pore spaces between grains, rather than fractures. Both studies used an intuitive analytical model derived from Aitken (1985) via Hofmann (1992). This model combines measured U, Th and K abundances, their activities, and reference data for the expected H_2 yield from water per energy absorbed (Spinks and Woods, 1990). It accounts for the attenuation of radiation energy within the bulk medium by factoring in the radiation stopping power of water, the stopping power of the mineral grains (assumed to equal that of silica, SiO_2, which has been experimentally determined for alpha, beta and gamma radiation), and the ratio of water to mineral matter by volume (i.e., porosity). Using this model, Lin et al. showed that radiolysis is the most likely cause of high H_2 concentrations measured in groundwaters of the Witwatersrand Basin in South Africa. They also modelled radiogenic ^{4}He production and compared the predicted H_2:He ratio with the empirically measured dissolved gas concentrations in Witwatersrand groundwater; the difference showed that H_2 was either produced less efficiently than the model predicted or was being consumed by a combination of abiotic reactions and hydrogenotrophic microorganisms. Onstott et al. (2006) adapted the model for Mars by substituting typical Martian values for crustal porosity and the concentration of parent nuclides. Assuming fully water-saturated basement, H_2 production rates were found to be comparable to crystalline basement on Earth because of the higher porosity of Mars' crust, despite the lower concentrations of uranium and thorium. Updated (higher) radionuclide concentrations were used by Tarnas et al. (2018, 2021) to estimate an even greater rate of radiolytic H_2 production on Mars, using the same model. Bouquet et al. (2017) applied a similar model to Jupiter's moon, Europa. Dzaugis et al. (2016) introduced a model of radiolytic H_2 production from water hosted within planar fractures in radioactive rock, rather than intergranular pore spaces, and applied it to subseafloor basaltic basement. Dzaugis et al. (2018) showed that this fracture-based model yields radiolytic H_2 production rates for Martian basaltic crust broadly comparable to those predicted for fine-grained Martian sediments by the model of Blair et al. (2017). One implication of these studies, in agreement with other considerations, is that the best place to seek extant life on Mars today is probably the subsurface (e.g., Tarnas et al., 2021).

Hitherto, studies of porewater radiolysis have not properly accounted for the attenuation of each radiogenic particle or ray within its mineral grain (clast or crystal) of origin. This attenuation can be safely ignored when the grain diameter is much smaller than the stopping distance of the relevant particle in the mineral medium, as for example in clay. However, alpha particles in the kinetic energy range characteristic of mineral radiation (~5.6 MeV on average) typically have stopping distances in SiO_2 (and similar materials) of ~23 μm (National Institute of Standards and Technology, 2021a). Consequently, if such an alpha particle is produced near the edge of a grain of diameter $\gtrsim$20 μm (i.e., coarser than a medium silt) and travels towards the interior of the grain, it will not have enough kinetic energy to escape from the other side, resulting in a null contribution to the radiolysis of the surrounding porewater. Similar considerations apply to beta particles—although their stopping distances are substantially larger—given a characteristic mean kinetic energy of ~0.33 MeV, equating to a stopping distance of ~452 μm in SiO_2 (National Institute of Standards and Technology, 2021b). Furthermore, the radiolysis contribution due to gamma (photon) radiation requires special treatment given their chargeless, massless character. Here, we quantitatively account for the variability of grain size in

order to expand the range of environments in which radiolytic H_2 production and its potential contribution to microbial productivity can be estimated. The method detailed in this paper is generalizable to the extent that it can be adapted for a variety of geological contexts and sediment or rock types with any level of radioactivity, whose constituent grains can be of arbitrary size and shape. In this particular study, we seek to model radiolytic H_2 production from porous rocks and sediments with grain sizes $\gtrsim$20 μm for the first time (to our knowledge). One motivation for doing so is the fact that high concentrations of radioactive minerals on Earth commonly occur in relatively coarse sedimentary rocks, e.g., sandstone-type uranium deposits. In addition, relatively coarse granular materials can accommodate more microorganisms, which may tend to be excluded by the restrictive pore throat sizes of finer-grained materials, even at the same porosity (e.g., Krumholz et al., 1997).

2 Materials and Methods

We have written a Fortran program that numerically simulates the physics of natural radioactive decay within a matrix of water and mineral grains, which for simplicity are assumed to be spherical and composed of pure SiO_2. (The algorithmic foundation of this program is given in Supplementary Information S1.) The modeling of spherical grains allows one to leverage the rotational symmetry of the system, which has the effect of easing the conceptual and computational aspects of the Monte Carlo (MC) method. The primary goal of our simulations is to score the total amount of kinetic energy transferred to the surrounding water layer due to the decay of radioactive isotopes within SiO_2 grains. Figure 1 shows the geometry of a spherical SiO_2 grain and a composite of sample thorium decay events occurring within it.

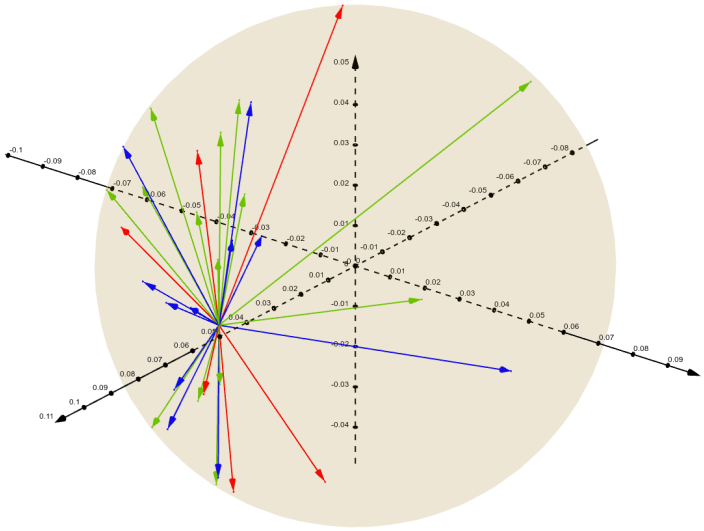


Figure 1. A randomly selected SiO_2 grain of radius 0.059 cm (590 μm) showing a sample thorium decay against x, y and z co-ordinate axes (black arrows with gradations). Alpha, beta,

and gamma decay events register as red, green, and blue, respectively. These depth vectors locate exit points that correspond to solutions of the sphere $r^2 = x^2 + y^2 + z^2$.

The program leverages the MC method and the physics of radioactive decay to drive a given simulation towards a well-averaged endpoint. The steps the simulation uses are as follows:

1. Choose a random SiO_2 grain whose radius is within the desired interval of clay, silt, or sand (Wentworth, 1922), or a logarithmic distribution of all three;
2. Choose a random K, Th, or U constituent (weighted by the proportion of that element in the composition; see "Activity of Bulk Rock or Sediment" below);
3. Choose a random point (x, y, z) within the grain at which the decay of the constituent plus its daughters will proceed;
4. Examine the entire decay chain in order, choosing random exit vectors, and applying the appropriate physics of alpha, beta, and gamma propagation in SiO_2;
5. Repeat Steps 1 – 4 many times (typically 10^5 trials) in order to ensure the simulation converges while keeping a running total of the amount of kinetic energy (in MeV) deposited in the surrounding water layer;
6. Output radiolytic H_2 production from the volume of rock or sediment;
7. Using Step 6 as a baseline, scale H_2 production by volume-corrected porosity (see "Porosity" below). Athy's law can be used to scale radiolytic H_2 production in the case where porosity can be estimated for a column of rock or sediment as a function of depth.

The "length" of the simulation is controlled by the number of K, Th, and U decays + daughters that are tracked (read: trials), with the understanding that a large number of trials will enable the simulation to converge in a manner dictated by the physics of radioactive decay. For the purposes of this study, our simulations output 1) H_2 production in units of moles per [Earth] year-cm^3 as a function of sediment depth in meters, or 2) H_2 production as a function of grain size (logarithmically distributed) in cm.

2.1 Radioactive decay

This section describes how the components of natural radioactivity interact with the medium through which they are propagating. This is also referred to as *stopping power* or *linear energy transfer* (LET). Our simulations treat alpha, beta, and gamma decay piecewise, wherein each decay daughter in a given chain is assigned a random exit vector. The entire decay chains for ^{238}U, ^{235}U, ^{232}Th, and ^{40}K were hard-coded into the program using data from the Interactive Chart of Nuclides provided by Brookhaven National Laboratory (2021). (The *average* energies required for each transition within a given decay chain were implemented rather than the "endpoint" or maximum energies, as previous studies have done.) These vectors are then used to propagate each decay product through a geometrically-computed depth of SiO_2 material before depositing the remainder of its kinetic energy in the surrounding water layer. This strategy is advantageous since it avoids the assumption of alpha, beta, and gamma dominance through the use of lump energy sums (Blair et al., 2007).

2.1.1 Alpha particles

The interaction of a heavy charged projectile with the electrons in a stopping medium (absorber) is described by the Bethe-Bloch formula (Bethe, 1930). The amount of kinetic energy $\mathrm{d}E$ imparted to the target medium per unit path length $\mathrm{d}x$ is given as

$$-\left\langle \frac{\mathrm{d}E}{\mathrm{d}x} \right\rangle = \underbrace{\left(\frac{e^2}{4\pi\epsilon_0} \right)^2}_{\text{Coulomb}} \underbrace{\frac{4\pi Z^2}{m_\mathrm{e} c^2 \beta^2}}_{\text{projectile}} \underbrace{\frac{\rho \bar{Z} N_\mathrm{A}}{\bar{A}}}_{\text{target}} \left[\ln\left(\frac{2 m_\mathrm{e} c^2 \beta^2}{I(1-\beta^2)} \right) - \beta^2 - \frac{\delta}{2} \right] \quad (1)$$

where $e^2/4\pi\epsilon_0$ is the coupling strength of electromagnetism, Z is the atomic number of the charged particle or ion projectile, $m_\mathrm{e}c^2$ is the rest mass-energy of the electron, $\rho\bar{Z}N_\mathrm{A}/\bar{A}$ is the electron density of the absorber with effective atomic number $\bar{Z}$ and effective atomic mass $\bar{A}$ (when referring to compounds and mixtures), and I is the mean ionization potential of the target medium. The dimensionless number $\beta \equiv v/c = \sqrt{1 - [m_\mathrm{e}c^2/(E + m_\mathrm{e}c^2)]^2}$ from special relativity. The last term in the square brackets $\delta/2$ is the *density effect correction* that accounts for the phenomenon that, in a dense medium, the field which perturbs electrons far from the projectile track is modified by the dielectric polarization of the atoms between the distant electrons and the projectile (Fermi, 1940). The quantity $\mathrm{d}E/\mathrm{d}x$ in Equation 1 is sometimes preceded by a negative sign to indicate that kinetic energy is transferred to the stopping medium.

Alpha particles (helium nuclei, Z = 2) that are emitted during the course of natural radioactive decay possess an average kinetic energy that is relatively low, or ~5.6 MeV. This low kinetic energy necessitates a correction to the stopping power due to the phenomenon of *electron capture*, which accounts for the fact that the bare nuclear charge of the projectile is reduced and can thus be replaced by an effective projectile charge (Weaver and Westphal, 2002). Once corrected, Equation 1 is used to numerically propagate alpha particles through a known amount of SiO_2 with characteristics $\rho\bar{Z}N_\mathrm{A}/\bar{A}$ and I.

A charged particle or ion projectile with atomic number Z of rest mass significantly larger than that of the electron (charge e) is considered a "heavy" charged particle. This would include mesons, protons, alpha particles, and higher Z nuclei. Electrons and positrons are considered "light" charged particles; the physics of electron propagation through matter is discussed in the next section.

2.1.2 Beta particles

While the Bethe-Bloch formula can be used in principle to calculate the stopping power of any charged particle passing through matter, it must be modified in the case of beta particles (electrons). There are several reasons for this:

- one must always consider special relativity when handling electron-electron interactions;
- an electron that acts as a projectile can lose nearly all of its kinetic energy in a single interaction with a target electron;
- quantum mechanics states that we will not be able to distinguish between the projectile and the target electrons after the *collision* (they are identical particles);
- for a high energy electron that traverses a high $\bar{Z}$ stopping medium, radiative processes such as *bremsstrahlung* (from the German: "breaking radiation") will be significant.

The total stopping power of an electron as a function of kinetic energy in a specified target material is the sum of the collision plus bremsstrahlung contributions (Bethe and Heitler, 1934):

$$\left\langle \frac{\mathrm{d}E}{\mathrm{d}x} \right\rangle = \left\langle \frac{\mathrm{d}E}{\mathrm{d}x} \right\rangle_{\mathrm{c}} + \left\langle \frac{\mathrm{d}E}{\mathrm{d}x} \right\rangle_{\mathrm{b}}, \tag{2}$$

where $\langle \mathrm{d}E/\mathrm{d}x \rangle_{\mathrm{c}}$ is the stopping power due to electron collisions,

$$\overbrace{-\left\langle \frac{\mathrm{d}E}{\mathrm{d}x} \right\rangle_{\mathrm{c}}}^{\text{collision}} = \overbrace{\left(\frac{e^2}{4\pi\epsilon_0} \right)^2}^{\text{Coulomb}} \overbrace{\frac{2\pi}{m_{\mathrm{e}} c^2 \beta^2}}^{\text{projectile}} \overbrace{\frac{\rho Z N_{\mathrm{A}}}{\bar{A}}}^{\text{target}}$$
$$\times \left[\ln\left(\frac{E(E + m_{\mathrm{e}}c^2)^2 \beta^2}{2I^2 m_{\mathrm{e}} c^2} \right) - \beta^2 + 1 - \left(2\sqrt{1-\beta^2} + \beta^2 - 1 \right) \ln 2 + \frac{1}{8} \left(1 - \sqrt{1-\beta^2} \right)^2 \right]$$
, (3)

and $\langle \mathrm{d}E/\mathrm{d}x \rangle_{\mathrm{b}}$ is the stopping power due to electron bremsstrahlung,

$$\underbrace{-\left\langle \frac{\mathrm{d}E}{\mathrm{d}x} \right\rangle_{\mathrm{b}}}_{\text{bremsstrahlung}} = \underbrace{\left(\frac{e^2}{4\pi\epsilon_0} \right)^2}_{\text{Coulomb}} \underbrace{\frac{\alpha(E + m_{\mathrm{e}}c^2)}{(m_{\mathrm{e}}c^2)^2}}_{\text{projectile}} \underbrace{\frac{\rho \bar{Z}^2 N_{\mathrm{A}}}{\bar{A}}}_{\text{target}} \left[4 \ln \left(\frac{2(E + m_{\mathrm{e}}c^2)}{m_{\mathrm{e}}c^2} \right) - \frac{4}{3} \right] \quad (4)$$

,

where α is the fine-structure constant. Equations 2-4 are used to numerically propagate beta particles through a known amount of SiO_2 with characteristics similar to those described by Equation 1.

The simulation of radioactive decay in a mineral medium requires that Equations 1-4 be applied to the propagation of alpha and beta particles inside spherical SiO_2 grains. As a means of developing and validating our numerical method, it would be well if the algorithm given in Supplementary Information S1 were checked against a pure geometric argument. To this end, we have found analytically that if particles with stopping distance s are emitted at random vectors from points inside a spherical grain of diameter Θ, the proportion (or percent fraction) of these particles that escape from the grain rather than terminating (or stopping) within it is given by

$$E_{\mathrm{g}}(\Theta) = \frac{3s}{2\Theta} - \frac{s^3}{2\Theta^3}. \quad (5)$$

Equation 5 is derived in Supplementary Information S2. Figure 2 shows a graphical comparison of these two methods in the case of alpha particles, along with an extension to beta particles using the same algorithm given in Supplementary Information S1.

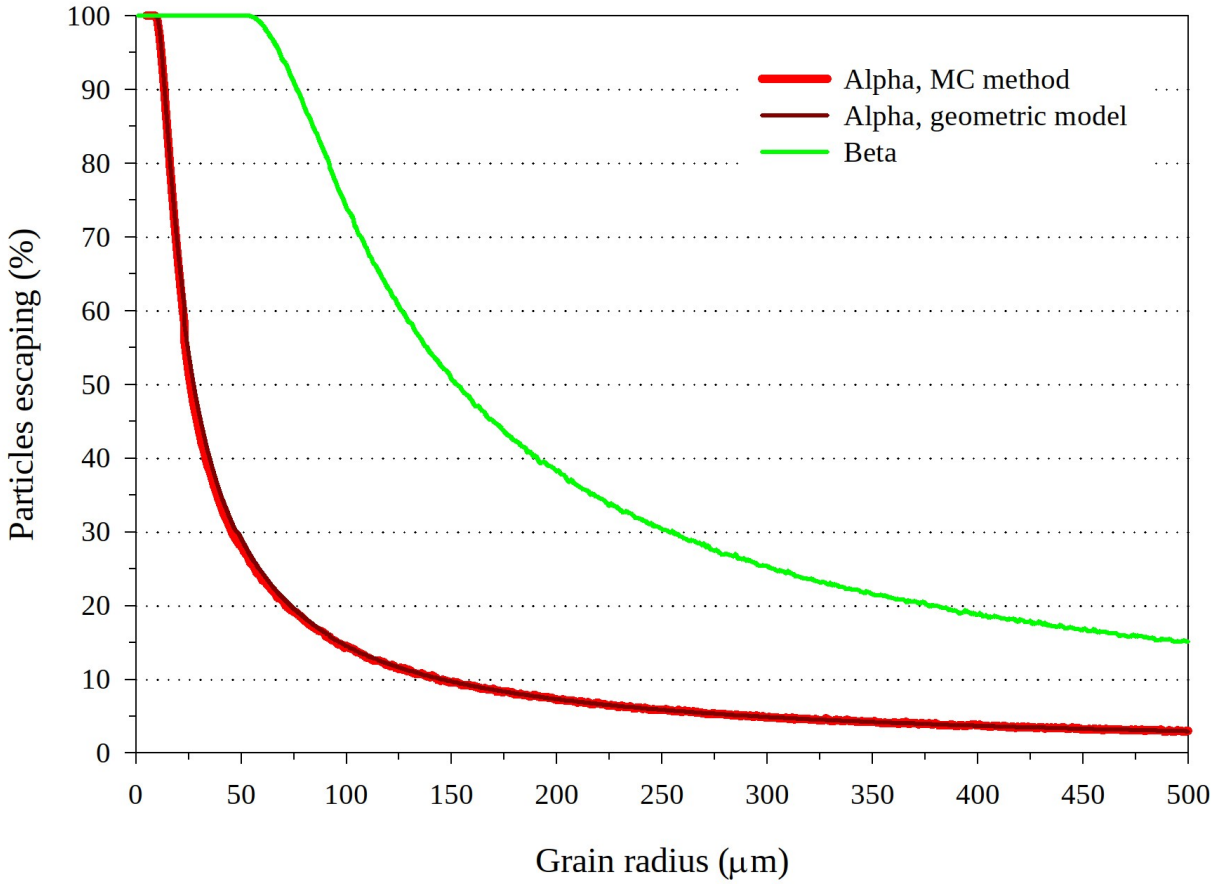


Figure 2. Escape efficiency of alpha particles with stopping distance s = 19.6 μm as a function of spherical grain radius, where the methods of Monte Carlo simulation and geometric analysis are compared. The escape efficiency of beta particles is also shown using the same algorithm.

The comparison shown in Figure 2 corresponds to an alpha particle test case with stopping distance s = 19.6 μm (kinetic energy: 4.93 MeV). These curves disagree on average by 0.2% over 100,000 trials per micron radius. The good agreement between the core algorithm of the simulation and our geometric analysis partially validates our MC approach in this study.

2.1.3 Gamma Rays

Unlike energetic charged particles which have a finite range when traversing matter, gamma rays (photons) of a given energy do not possess such a discrete range, but rather are absorbed exponentially as a function of distance in the absorbing medium. This phenomenon is referred to as *attenuation*. (Alpha and beta particles, strictly speaking, do not attenuate; we use this term contextually to service the reader.) For a beam of n_0 monoenergetic photons, the rate of absorption of the photons as a function of depth in the absorber is

$$-\frac{\mathrm{d}n}{\mathrm{d}x} = N\sigma n_0, \tag{6}$$

where σ is the absorption cross section of each atomic scattering center (or absorbing molecule), and N is the volume density of atomic scattering centers. (The negative sign above represents absorption.) We define $\mu \equiv N\sigma$, where μ is referred to as the *linear attenuation coefficient*. We can then integrate Equation 6 with respect to distance x to obtain

$$n(x) = n_0 \mathrm{e}^{-\mu x}. \tag{7}$$

Similarly, if we consider depth x in terms of not distance, but of areal density (in g/cm^2), we can define the *mass attenuation coefficient* such that

$$\mu_\mathrm{m} \equiv \frac{\mu}{\rho} = \frac{N\sigma}{\rho} = \frac{N_\mathrm{A}\sigma}{\bar{A}}, \tag{8}$$

where ρ is the mass density (in g/cm^3), $\bar{A}$ is the atomic molar mass (in g/mol) of the absorbing medium, and N_A is Avogadro's number (in molecules/mol), respectively. Equation 7 now becomes

$$n(x) = n_0 \mathrm{e}^{-\mu_\mathrm{m} x}, \tag{9}$$

where the values of μ_m are tabulated.

Using Equation 9, a characteristic *attenuation* (or *absorption*) *length* can be formulated as an analog to the stopping distance of alpha and beta particles; for a single photon, this is taken as the distance x into a material when the probability of absorption has dropped to $n/n_0 = 1/\mathrm{e}$, or ~37%. Explicitly, this gives a propagation distance that is equal to the inverse of the mass attenuation coefficient, or $1/\mu_\mathrm{m}$. A typical attenuation length in this study is on the order of centimeters.

There are a number of different mechanisms by which photons can interact with matter. However, only three of these mechanisms—the photoelectric effect, Compton scattering, and electron/positron pair production—dominate, while the remainder usually make only a negligible contribution. The total absorption cross section σ in Equation 8 is the sum of the cross sections for each type of photon interaction:

$$\sigma = \sigma_\mathrm{PE} + \sigma_\mathrm{C} + \sigma_\mathrm{PP}, \tag{10}$$

where σ_{PE} is the cross section for photoelectric interactions, σ_{C} is the cross section for Compton interactions, and σ_{PP} is the cross section for pair production. (A cross section in nuclear physics can informally be read as an energy-dependent probability for interaction.) Since $\mu \propto \sigma$ from Equation 8, there is a corresponding mass attenuation coefficient for each cross section.

2.1.3.1 Photoelectric Effect

Free electrons cannot fully absorb photons without violating conservation of energy and conservation of momentum, and for that reason, free electrons are not subject to the photoelectric effect. Indeed, the photoelectric effect should be thought of as interaction between an incident photon and an entire atom, not just one of its electrons (Einstein, 1905).

Photoelectric interactions are more likely to eject electrons from the more tightly bound inner electron shells of the atom than the less tightly bound outer shells, since interactions involving inner shell electrons occur closer to the center of the atom where it is easier to transfer an incident photon's linear momentum to the atom. This is because nearly all the mass of the atom is concentrated in its nucleus.

The cross section for the photoelectric effect is:

$$\sigma_{\mathrm{PE}} = 4\sqrt{2}\alpha^4 \bar{Z}^5 \frac{8\pi r_{\mathrm{e}}^2}{3} \left(\frac{m_{\mathrm{e}} c^2}{E_\gamma} \right)^{7/2}, \tag{11}$$

where α is the fine-structure constant, $\bar{Z}$ is the atomic number of the absorbing medium, r_{e} is the classical electron radius, the quantity $m_{\mathrm{e}}c^2$ is the rest mass-energy of the electron, and finally E_γ is the kinetic energy of the incident photon. Equation 11 should be applied if the energy of the incident photon is between 0.1 and 0.35 MeV, or where the photon energy is above the K-absorption edge.

2.1.3.2 Compton Scattering

The interaction of photons with "nearly" free electrons is described by a number of mechanisms:

- Photon interactions with "truly" free electrons is referred to as *Thomson scattering*;
- Coherent (or elastic) photon interactions with "nearly" free electrons is referred to as *Rayleigh scattering*;
- Incoherent (or inelastic) photon interactions with "nearly" free electrons is referred to as *Compton scattering*.

Conservation of energy for the Compton scattering interaction gives

$$E_\gamma + m_\mathrm{e}c^2 = E'_\gamma + \frac{m_\mathrm{e}c^2}{\sqrt{1-\beta^2}}, \tag{12}$$

where $\beta \equiv v/c = \sqrt{1 - \left[m_\mathrm{e}c^2/(E_\gamma - E'_\gamma + m_\mathrm{e}c^2)\right]^2}$ from special relativity, with E_γ and E'_γ the kinetic energies of the incident and scattered photon, respectively. After obtaining the differential cross section for Compton scattering—which is specified by the Klein-Nishina formula (Klein and Nishina, 1929)—it can be shown that integration over all angles gives the cross section for the Compton interaction:

$$\sigma_\mathrm{C} = \frac{\pi r_\mathrm{e}^2}{\bar{E}}\left[\left(1 - \frac{2(\bar{E}+1)}{\bar{E}^2}\right)\ln(2\bar{E}+1) + \frac{1}{2} + \frac{4}{\bar{E}} - \frac{1}{2(2\bar{E}+1)^2}\right], \tag{13}$$

where $\bar{E}$ effectively compares the incident photon energy to the rest mass-energy of the electron, or $E_\gamma/m_\mathrm{e}c^2$.

2.1.3.3 Pair Production

Pair production is essentially the reverse process of bremsstrahlung. When in close proximity to a heavy nucleus, a photon can be converted into an electron/positron pair. Conservation of energy for this process dictates

$$E_\gamma = T_\mathrm{e} + m_\mathrm{e}c^2 + T_\mathrm{p} + m_\mathrm{e}c^2, \tag{14}$$

where T_e and T_p are the kinetic energy of the electron and positron, respectively. Because the rest mass of the electron and the positron must come from the energy of the photon, there is a threshold energy of $2m_\mathrm{e}c^2$ = 1.022 MeV below which this process cannot occur.

The cross section for pair production originates from quantum electrodynamics, and is given by (Gould and Schréder, 1967):

$$\sigma_\mathrm{PP} = \frac{\pi r_\mathrm{e}^2}{2}(1-\beta^2)\left[(3-\beta^4)\ln\left(\frac{1+\beta}{1-\beta}\right) - 2\beta(2-\beta^2)\right], \tag{15}$$

where $\beta \equiv v/c = \sqrt{1 - \left[m_\mathrm{e}c^2/(E + m_\mathrm{e}c^2)\right]^2}$ from special relativity. In this case E is actually the relativistic kinetic energy of the electron/positron in the center-of-mass frame of reference. This cross section is applied for the transitions $^{40}\mathrm{K} \rightarrow {}^{40}\mathrm{Ar}$ in ^{40}K (1.461 MeV), $^{208}\mathrm{Tl} \rightarrow {}^{208}\mathrm{Pb}$ in ^{232}Th (3.376 MeV), and $^{214}\mathrm{Bi} \rightarrow {}^{214}\mathrm{Po}$ in ^{238}U (1.476 MeV).

354

355 2.2 Activity of Bulk Rock or Sediment

356 The activity per unit volume A_{vol} of bulk rock/sediment in units of Bq/cm^3 is given by
357

$$A_{\mathrm{vol}}(\rho, N_{\mathrm{ppm}}) = \frac{\rho N_{\mathrm{A}}}{M} \frac{N_{\mathrm{ppm}}}{10^6} \frac{\ln(2)}{t_{1/2}}, \tag{16}$$

358

359 where ρ is the mass density of the rock/sediment constituents in g/cm^3, N_{A} is the Avogadro
360 constant, M is the molar mass of the radioisotope, N_{ppm} is the concentration of the radioisotope
361 in parts per million (ppm), and $t_{1/2}$ is the half-life of the radioisotope in seconds. Equation 16 is
362 used to convert the concentration of a given radioisotope component (uranium, thorium, or
363 potassium) to the volume-normalized activity in bulk sediment/rock. For example, sediment of
364 mass density 2.6 g/cm^3 that contains radioisotope concentrations of uranium (7.4 ppm), thorium
365 (2.8 ppm), and potassium (1.3%) results in A_{vol} values of 0.24, 0.030, and 1.1 Bq/cm^3,
366 respectively, using Equation 16 and the data given in Table 1. Recognizing also that ^{235}U
367 contributes to the overall activity (0.011 Bq/cm^3), the total activity per unit volume of the
368 sediment is simply the sum of the individual activities, or ~1.4 Bq/cm^3.

369

370 **Table 1.** A summary of radioisotopes relevant to natural radioactive decay in minerals.

Radioactive Isotope	Molar Mass, M (g/mol)	Half-life, $t_{1/2}$ (s)
^{238}U (99.274%)	238.0508	1.4090E17
^{235}U (0.720%)	235.0439	2.2195E16
^{232}Th	232.0381	4.4308E17
^{40}K (0.0117% of ^{40}K in ^{39}K)	39.0983	3.9452E16

371 From an MC perspective, it is helpful to convert the A_{vol} values above to algorithm-
372 friendly percent fractions of roughly 18%, 1%, 2%, and 79% for ^{238}U, ^{235}U, ^{232}Th, and ^{40}K,
373 respectively. Through this example we can see that a random number generator will select
374 potassium predominantly over the course of a given simulation.

375

376 2.3 Porosity

377 A porosity correction is needed to account for the fact that only the kinetic energy
378 deposited in the intergranular water (rather than other grains) will contribute to H_2 production.
379 The porosity of a compressible rock or sediment column decreases with increasing depth as the
380 grains are compacted together. The simulations presented in this paper assume that all the
381 porosity is occupied by water; we use Athy's law to quantify porosity ϕ as a function of sediment
382 (or rock) depth z (Fowler and Yang, 1998):

383

$$\phi(z) = \phi_0 \mathrm{e}^{-kz}, \tag{17}$$

where ϕ_0 is the porosity near the surface and k is the compaction coefficient and has units of m^{-1}. In sandstones on Earth, k takes an average value close to 5.3E-4 m^{-1} (McMahon and Parnell, 2014); for geological features on Mars, this study uses a slightly lower compaction coefficient of 3.5E-4 m^{-1} (Clifford et al., 2010). Equation 17 represents a steady-state leading-order solution to equilibrium compaction.

A volume correction factor is required to properly scale H_2 production as a function of depth. This factor, $1 - \phi_0$, accounts for the fact that in a given volume of rock/sediment, a large porosity will translate to a smaller proportion being occupied by radioactive mineral grains rather than water. The kinetic energy yield from a given volume of wet rock/sediment is equal to the energy yield of each grain (supplied by the simulation) multiplied by the total number of grains contained in the volume. This total grain number is equal to the volume of the rock/sediment multiplied by a factor of $1 - \phi_0$, normalized by the volume of each grain (Blair et al., 2007). Given this, it is necessary to replace ϕ_0 in Equation 17 with $\phi_0(1 - \phi_0)$ to give an effective porosity as a function of rock/sediment depth.

In this study, Athy's law is implemented as a multiplicative factor that scales the hydrogen production by water radiolysis model of Blair and coworkers (Blair et al., 2007):

$$P_{\text{sed}} = P_\alpha + P_\beta + P_\gamma = G_\alpha E_\alpha + G_\beta E_\beta + G_\gamma E_\gamma, \tag{18}$$

where G_α, G_β, and G_γ are the H_2 yields per unit kinetic energy produced in pure water by radiolysis, and E_α, E_β, and E_γ are the kinetic energies absorbed by water in bulk rock/sediment due to alpha, beta, and gamma decay, respectively. The values of G_α, G_β, and G_γ are 1.57E4, 5.30E3, and 4.50E3 molecules/MeV, respectively (Spinks and Woods, 1990; Blair et al., 2007); the values of E_α, E_β, and E_γ (in MeV) are determined by the simulation.

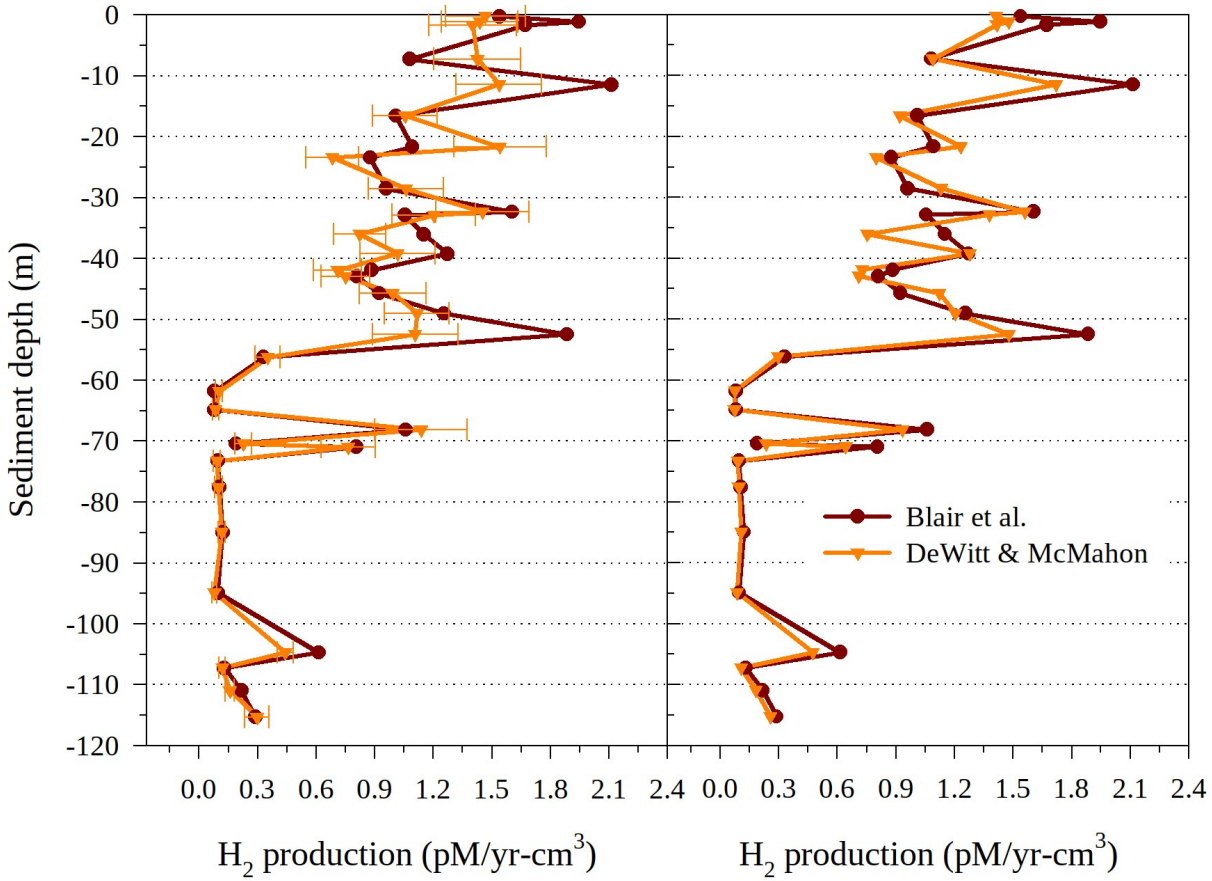


Figure 3. A comparison of the predicted radiolytic hydrogen flux using the MC method (orange line) with the analytic model of Blair et al. (2007) using the radionuclide concentrations, grain sizes, and porosities reported for a marine sediment column sampled by the Ocean Drilling Program in the Peru Basin. The left panel shows the anticipated H_2 production after 200 trials, while the right panel shows the same after 200,000 trials. The differences between the predictions of Blair et al. and this study are methodological and do not relate to grain size effects.

Figure 3 compares the predicted H_2 production given by the MC method with those calculated by Blair et al. (2007) from marine sediment column measurements as a function of depth. This figure demonstrates the compatibility of our simulations with the deep marine sediment column in which empirically-determined radionuclide concentrations, grain sizes, and porosities (measured by the Ocean Drilling Program in the Peru Basin) were provided by Blair and coworkers. The left panel in Figure 3 displays a comparison after 200 MC trials, while the right panel shows the same after 200,000 trials. In general, this figure shows that the MC method accurately reproduces the calculations of Blair et al. where confidence is high (i.e., standard error is low); any disagreement above ~55 meters is be attributed to 1) the error in measured ^{232}Th concentrations, and 2) the differing decay energy sums of the two approaches. (Whereas Blair et al. used the endpoint, or maximum, decay energies within a given chain, this study used instead

the average to better represent the spectrum of possible outcomes). Finally, it should be noted that the grain sizes, with an average diameter of 6.2 μm over 120 meters, are too small in this case to attenuate the modelled flux.

3. Results

3.1 Effects of Grain Size

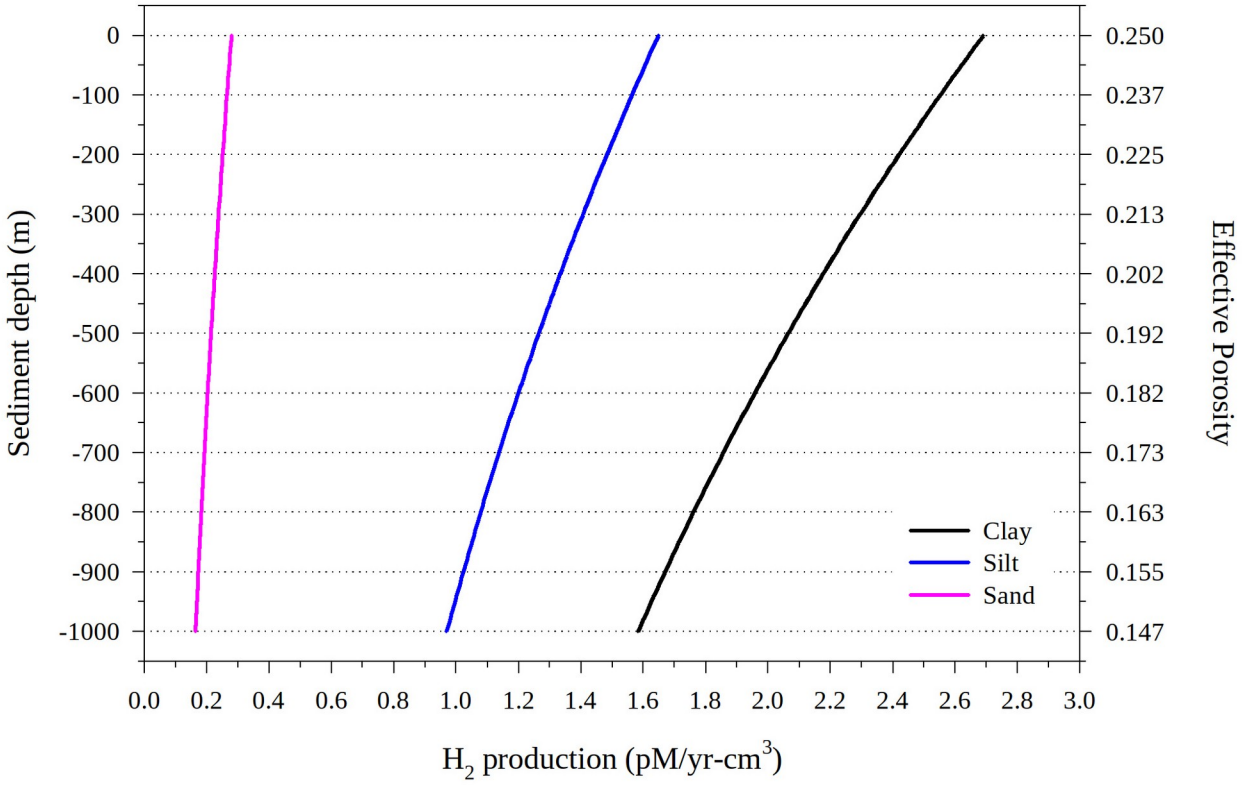


Figure 4. Radiolytic hydrogen production as a function of sediment (or rock) depth for the test case of 7.4 ppm U, 2.8 ppm Th, and 1.3% K, with ϕ_0 = 0.5 and k = 5.3E-4 m^{-1}. The SiO_2 grain size is sampled over clay (0.06 - 3.9 μm), silt (3.9 - 63 μm), and sand (63 - 2,000 μm). (In this simple model, porosity is independent of grain size.)

Figure 4 shows modelled H_2 production as a function of depth for the test case of 7.4 ppm U, 2.8 ppm Th, and 1.3% K (arbitrary but fairly typical values for geological materials) with ϕ_0 = 0.5 and k = 5.3E-4 m^{-1}; the grain size is randomly sampled over intervals corresponding to the grain sizes of clay (0.06 - 3.9 μm), silt (3.9 - 63 μm), and sand (63 - 2,000 μm). This figure incorporates the understanding that porosity of rock or sediment column—and therefore overall water content—increases nearer the surface while grain size is independent of depth. In general, these results show that the effect of grain size on H_2 flux is substantial.

446 Overall, Figure 4 demonstrates the extent to which radiolytic hydrogen production is
447 larger in smaller grains, and so largest in clay when compared with silt or sand. If alpha radiation
448 is used as a baseline with its comparatively large conversion coefficient (G_α, Equation 18), then
449 this can be understood in terms of an average stopping distance that is at least an entire order of
450 magnitude larger than a characteristic clay grain. By contrast, H_2 flux is reduced in silt-sized
451 grains, where characteristic grain sizes are comparable to the average stopping distance of alpha
452 radiation (~23 μm). In sand, the production of H_2 is reduced by an entire order of magnitude
453 compared to clay and silt. As before, this phenomenon can be understood in terms of
454 characteristic grain size versus stopping distance and/or attenuation length (in the case of gamma
455 emission). If the average stopping distance of beta radiation from natural radioactive decay is
456 ~452 μm, then there is the possibility that this decay mode—in conjunction with alpha—is also
457 strongly attenuated, thereby allowing the H_2 contribution due to gamma emission to dominate
458 (attenuation length: 3.2 cm or 32,000 μm).

459 It is clear from Figure 4 that the decrease in radiolytic hydrogen production as a function
460 of depth is due to Athy's law (Equation 17). Quantitatively, H_2 fluxes near the surface of 2.7, 1.6,
461 and 0.3 pM/yr-cm^3 in clay, silt, and sand, respectively are reduced to 1.6, 1.0, and 0.2 pM/yr-cm^3
462 at the maximum depth of 1 km. Moreover, using these values near the surface as a baseline, we
463 can see that the production of H_2 decreases by 41% in clay, silt, and sand at the maximum depth.
464 This reduction depends on the values of ϕ_0 and k in the functional form of Athy's law.

465

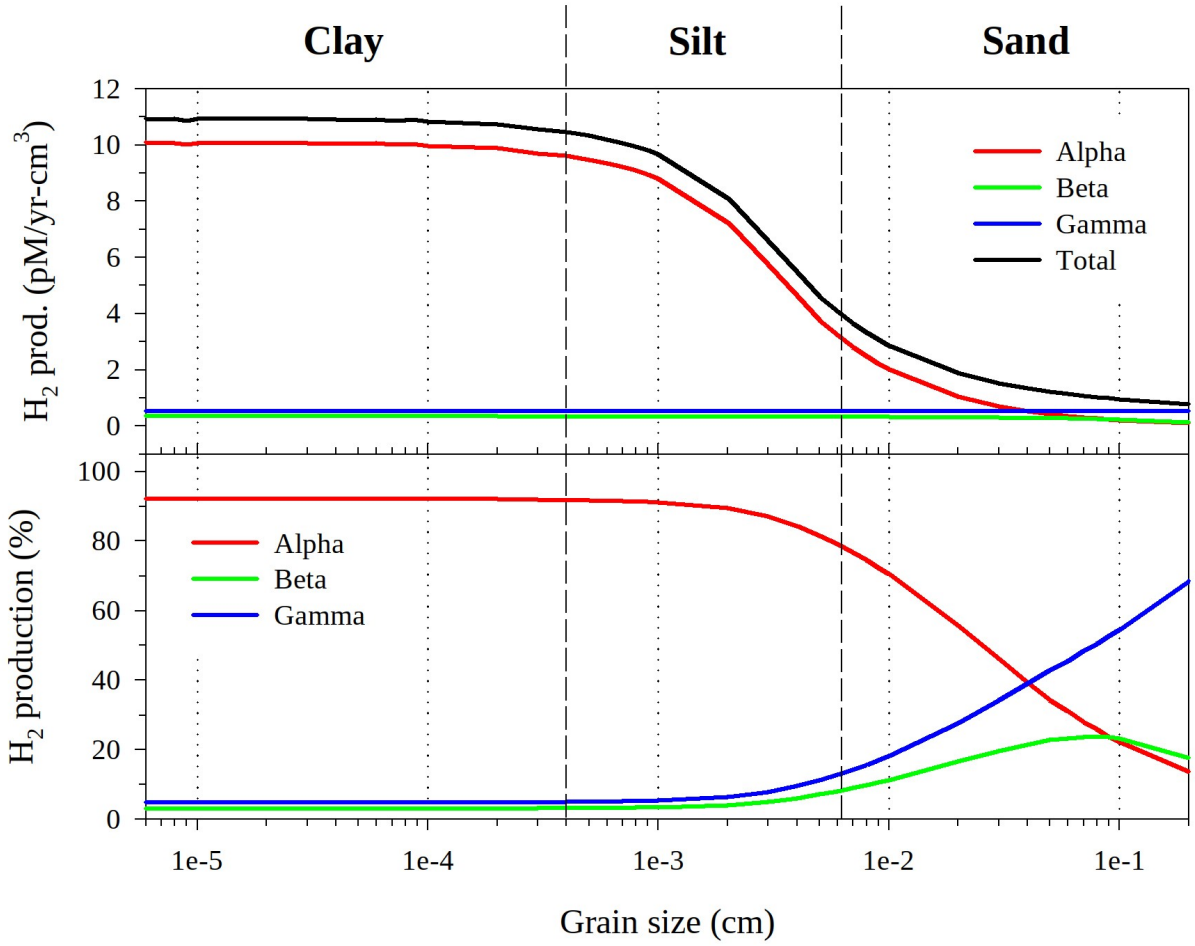


Figure 5. Radiolytic hydrogen production via alpha, beta, and gamma decay as a function of SiO_2 grain size for the test case of 7.4 ppm U, 2.8 ppm Th, and 1.3% K. Top: total H_2 production per unit volume of water-saturated sediment or rock. Bottom: percentage contribution of each type of radiation to the total H_2 yield.

Figure 5 compares the effect of grain size on H_2 production due to alpha, beta, and gamma radiation for the test case presented in Figure 4. (Neither the porosity correction nor the volume correction is applied here since neither would qualitatively alter the comparison.) The top panel shows H_2 production in units of pico (p, E-12) moles per [Earth] year-cm^3 as a function of SiO_2 grain radius in cm. Note that H_2 production due to alpha decay is strongly attenuated as a function of grain size. This phenomenon is explained by the relatively short average stopping distance of alphas (~23 μm or 2.3E-3 cm) compared to beta particles (electrons) and gamma rays (photons). Furthermore, this figure also shows that H_2 production due to alpha decay mirrors the total amount over a logarithmic distribution of grain sizes from clay to sand. This is due to the preponderance of alpha particles in the radioactive emissions of the simulated material, and to the high radiolytic H_2 yield per unit kinetic energy for alpha particles, which dominates that of beta particles and gamma rays by an entire order of magnitude (Spinks and Woods, 1990). Figure 5 (bottom) shows H_2 production in terms of percent fraction as a function of SiO_2 grain radius in cm. This figure (which would have to be adapted for simulations of materials with

different U, Th and K concentrations) is useful in detailing the relative contributions to H_2 production as a result of alpha, beta, and gamma decay in clay, silt, and sand. In general, Figure 5 suggests that the total H_2 production in this test water-SiO_2 matrix is dominated by the influence of alpha decay. Beta and gamma decay, by contrast, make relatively modest contributions, where little or no attenuation is observed.

In clay, H_2 production from alphas in this simulation is approximately constant at 10.0 ± 0.1 pM/yr-cm^3 where the grain size is smaller than the characteristic, or average, stopping distance as a result of natural radioactive decay. By contrast, H_2 production due to beta and gamma decay is comparatively small, with estimates of 0.3377 ± 0.0003 and 0.5220 ± 0.0002 pM/yr-cm^3, respectively. This is explained by the differing radiolytic H_2 yields per unit kinetic energy of these radiation types, i.e., G_α, G_β, and G_γ factors. The percent contributions in clay due to alpha, beta, and gamma decay are 92%, 3%, and 5%, respectively. The contribution from alpha decay is thus compatible with Blair et al. (2007), who report an estimate of 90 ± 2 % in the case of clay-like grain sizes and similar radioactivity levels. These simulations also indicate that the main radioisotope contributor in this particular test material is ^{238}U, with the remaining components of ^{235}U, ^{232}Th, and ^{40}K producing only trace amounts of H_2 irrespective of the decay mode. This figure shows that these percent contributions are roughly constant due to the comparatively weak attenuation of kinetic energy in the small grains characteristic of clay.

The difference in grain size between clay and silt translates into a marked decrease in H_2 yield by the latter. This is not surprising given that a typical alpha particle undergoing radioactive decay in SiO_2 will range on the order of E-3 cm. Figure 5 also shows that the degree of attenuation is substantial: The lower grain-size bound of silt due to alpha decay produces 9.6 pM/yr-cm^3, while the upper grain-size bound produces 3.2 pM/yr-cm^3. Similar to clay, H_2 production in silt due to beta and gamma radiation are virtually unchanged due to their comparatively large stopping distance and attenuation length, respectively. The effect of increased grain size is more readily apparent in the percent fractions of H_2 production due to alpha, beta, and gamma decay. At the lower grain-size bound of silt, alpha radiation is responsible for roughly 92% of H_2 production. This reduces to 79% at the upper bound, with the percent fractions of beta and gamma increasing to 8% and 13%, respectively, as a result.

In sand, the attenuation of alpha particles is more pronounced than that observed in silt. (It should be noted that the reduction of H_2 production in this test water-sand matrix qualitatively resembles the escape efficiency of alpha particles seen in Figure 2.) The lower bound of sand due to alpha decay produces 3.2 pM/yr-cm^3, while the upper bound produces 0.1 pM/yr-cm^3; between 1 and 2 mm grain size, the production of H_2 due to alpha and beta decay is comparable. The effect of alpha particle attenuation is readily apparent in sand, where the percent fraction contributions of beta and gamma radiation compensate proportionally. At the upper bound (~0.2 cm), alpha, beta, and gamma emissions contribute 14%, 18%, and 68% to H_2 production, respectively. Furthermore, a local maximum in the curve corresponding to beta decay is observed at ~0.08 cm, suggesting that beta particles “range-out” in grain sizes characteristic of sand. This is consistent with the average beta-particle stopping distance of ~0.05 cm in natural radioactive decay (National Institute of Standards and Technology, 2021b). No such maximum is observed in the curve corresponding to gamma radiation, however, owing to the comparatively large average attenuation length (~3.2 cm) of this decay mode in rock/sediment, not to mention the differing physics of photon propagation in matter. Given the grain sizes explored in this study, we have naturally found that all gamma radiation escapes from the originating grain.

3.2 Application to Natural Systems

Having validated our method for predicting the radiolytic hydrogen flux in clay, silt, and sand, in this section we consider how grain size could affect radiolytic yields from a variety of geologically interesting natural materials of known (or estimable) porosity and radionuclide concentration. Table 2 summarizes the values of key parameters (other than grain size) used here to simulate porewater radiolysis at Jezero Crater on Mars, the average upper continental crust of the Earth, monazite beach sand found in Ullal (India), the upper half of the Peru Basin sediment column examined in Figure 3, and Upper Vredefort Crust of South Africa.

Table 2. A summary of the input parameters used to generate Figures 6-10. The activities are computed using Equation 16 with a mass density of 2.7 g/cm^3. The total activity per unit volume of rock/sediment A_{tot} is the sum of all radioisotope contributions. We assume that hard, crystalline rocks have depth-invariant porosity since they are effectively incompressible over the depth range sampled (Gleeson et al., 2016). For the other geological settings, we set k, the compaction coefficient, to 5.3E-4 m^{-1} on Earth and 3.54 m^{-1} on Mars (Clifford et al. 2010).

Geological Formation	A_{tot} (Bq/cm^3)	$A_{40\text{-K}}$ (%)	$A_{232\text{-Th}}$ (%)	$A_{235\text{-U}}$ (%)	$A_{238\text{-U}}$ (%)	ϕ_0 (%)	k (m^{-1})	Reference
Jezero Crater, Mars	0.3	~96	$\gtrsim$2	<<1	$\lesssim$2	35	3.546 1E-4	Dzaugis et al. (2018) Clifford et al. (2010) for k
Upper continental crust (Earth, granitic)	2.2	~90	$\gtrsim$5	<1	$\gtrsim$4	1	0	Aquilina et al. (2004)
Monazite beach sediment, Ullal, India	6.4	~7	~77	<1	$\gtrsim$15	40	5.3E-4	Radhakrishna et al. (1993) except ϕ_0
Peru Basin sediment column	2.3	~86	$\gtrsim$7	<1	$\gtrsim$6	88	5.3E-4	Blair et al. (2007)
Upper Vredefort Crust	3.3	~92	$\gtrsim$5	<1	$\gtrsim$2	0.25	0	Lin et al. (2005)

549 The factor A_{tot} (decay/sec-cm^3) listed in Table 2 is used in part to convert the H_2
550 production of Equation 18 (molecules H_2 / decay) to units of M/yr-cm^3. The other activities listed
551 in this table serve as "probability selectors" for the Monte Carlo simulation. (For example, the
552 radioisotope ^{40}K, being relatively abundant in minerals, is commonly selected by the random
553 number generator.) The parameters ϕ_0 and k (surface porosity and compaction coefficient,
554 respectively) are used in Athy's law (Equation 17) to determine the effective sediment porosity
555 as a function of depth. For the upper half of the Peru Basin sediment column, we used the
556 average of the porosity measurements above ~55 meters to extrapolate this geological formation
557 to greater depths.

558 Similar to Figure 4, Figure 6 shows modelled H_2 production as a function of
559 sediment/rock depth for Jezero Crater on Mars, the upper continental crust of the Earth, monazite
560 beach sediment found in Ullal (India), the upper half of the Peru Basin sediment column
561 examined in Figure 3, and Upper Vredefort Crust of South Africa. As before, the grain size is
562 randomly sampled over intervals corresponding to clay (0.06 - 3.9 μm), silt (3.9 - 63 μm), and
563 sand (63 - 2,000 μm).

564 Regardless of grain size, Figure 6 demonstrates that radiolytic hydrogen flux is highest in
565 the monazite beach sediment of Ullal, India, and lowest in Upper Vredefort Crust of South
566 Africa, when nearest-neighbor effects in the form of porosity are considered. The observed
567 disparity between high and low is three orders of magnitude across clay, silt, and sand; the
568 ordering of these depth-flux curves appears to arise from a complex interplay of the factors given
569 in Table 2.

570 The effects of grain size on mineral radioactivity and radiolysis at a given depth can be
571 quantified by making a straightforward comparison of H_2 flux values at any depth (n.b., Athy's
572 law). Choosing values near the surface and the grain sizes of silt and sand—where characteristic
573 grain sizes attenuate alpha radiation—the ratio of relative change sand:silt reveals a factor of
574 2.30 ± 0.03 for the upper continental crust of the Earth, the upper half of the Peru Basin sediment
575 column, and Upper Vredefort Crust. (As a means of shorthand, we will refer to these geological
576 formations collectively as the "typical Earth group".) That is, H_2 production is reduced
577 consistently by about $\frac{3}{7}$ across geological formations of similar radioactivity when comparing silt
578 versus sand at a given depth. For the case of Jezero Crater on Mars, this factor is comparable, or
579 2.21. However, the unusual radioactive conditions found in the monazite beach sand of Ullal,
580 India produce a silt/sand "shifting" factor of 2.48, or about 7% more than elsewhere.
581 Furthermore, it should be noted that the combination of ϕ_0 and k on Mars result in a reduction of
582 H_2 production by 30% in all grain sizes at the maximum depth, which is lower than 41% in the
583 case of terrestrial conditions. In other words, the slopes of the depth-flux curves, when viewed in
584 semi-log space, are steeper.

585

586

587

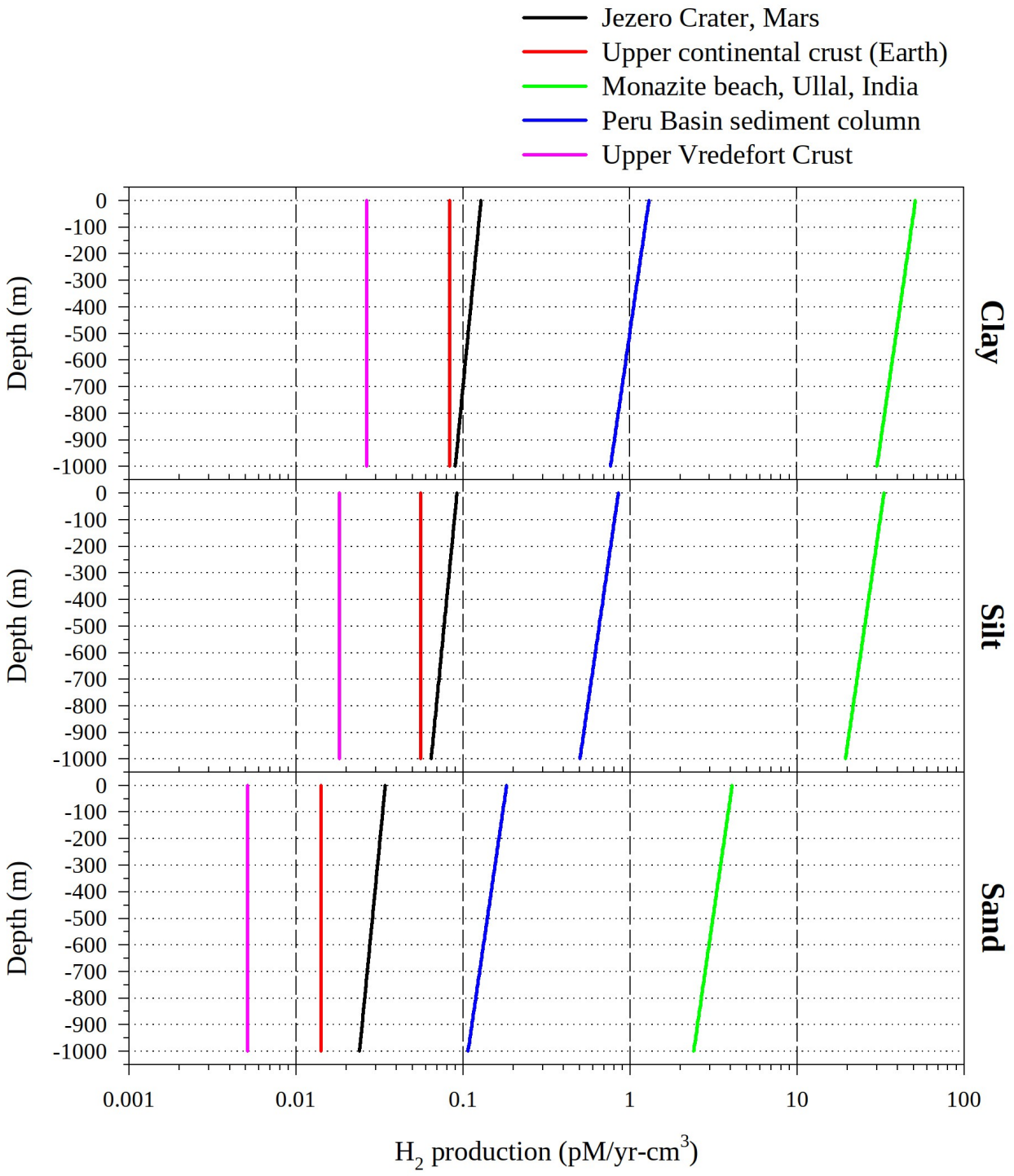


Figure 6. Radiolytic hydrogen production as a function of depth in a variety of geological settings. The SiO_2 grain size is sampled over clay (0.06 - 3.9 μm), silt (3.9 - 63 μm), and sand (63 - 2,000 μm).

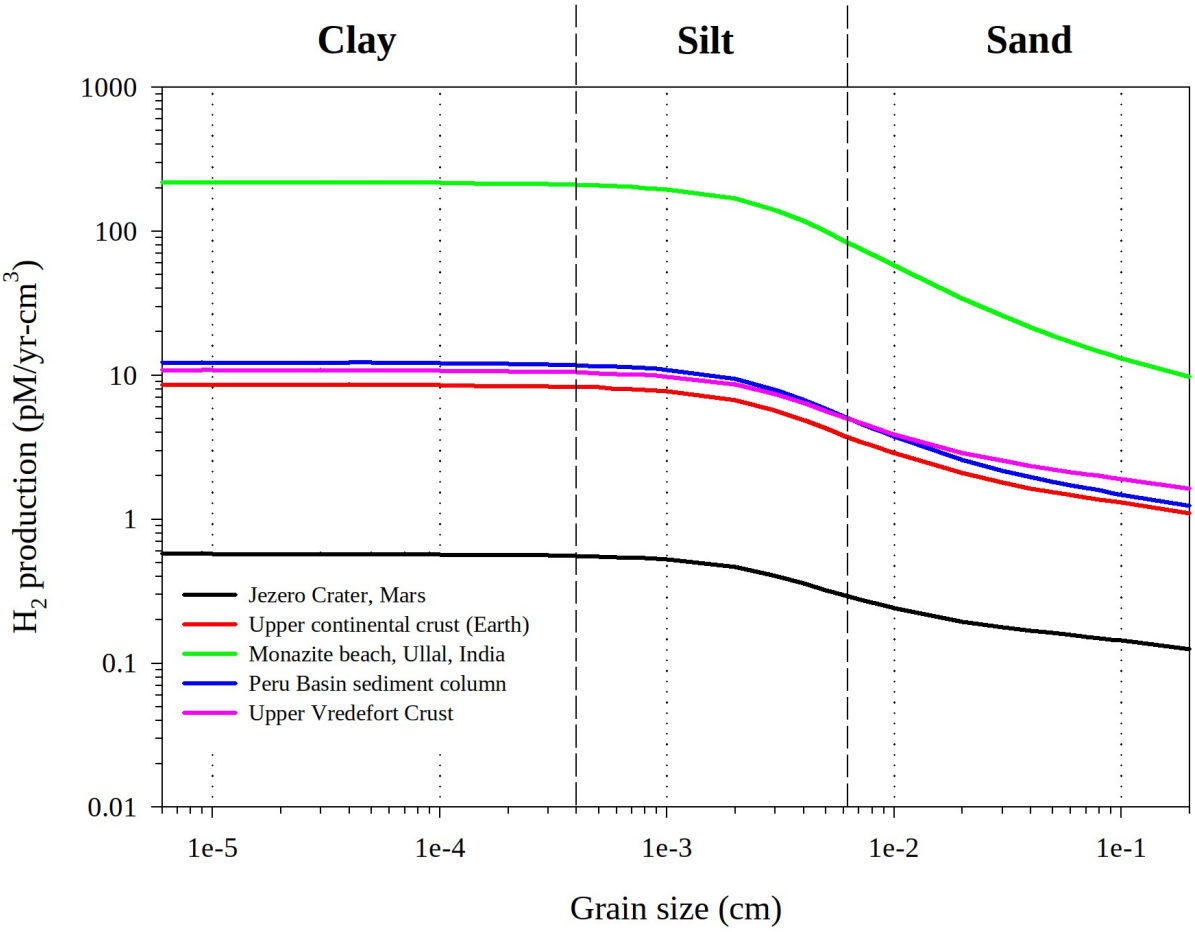


Figure 7. Total radiolytic hydrogen production (from **all sources**) as a function of SiO_2 grain size in a variety of geological formations.

Figure 7 shows total H_2 production in units of pico (p, E-12) moles per [Earth] year-cm^3 as a function of SiO_2 grain radius in cm for the geological formations presented in Figure 6. This figure shows that the monazite beach sand of Ullal, India produces an H_2 flux that is three orders of magnitude larger than Jezero Crater on Mars. Consistent with the observation in Figure 6, the typical Earth group predicts comparable fluxes of radiolytic hydrogen owing to their similar overall radioactivity. If monazite beach sand were reduced to a grain size in the range of clay, H_2 production from all sources of radiation would be approximately 216 ± 2 pM/yr-cm^3 (compared to 86 and 10 pM/yr-cm^3 at the upper bounds of silt and sand, respectively). This comparatively large H_2 flux stands in contrast to the typical Earth group, which displays an average of 10.5 ± 1.8 pM/yr-cm^3. At the lower end, Jezero Crater on Mars gives an estimate of 0.57 ± 0.01 pM/yr-cm^3. At the grain size of silt, the typical Earth group gives a reduced H_2 flux of 4.7 ± 0.8 pM/yr-cm^3 where grain sizes approach those characterizing sand (i.e., the upper bound of silt). Similarly, Jezero Crater reduces to 0.3 pM/yr-cm^3. The slope of the decline in H_2 flux with increasing grain size becomes shallower in sand. Specifically, at ~0.2 cm, radiolytic hydrogen production in the typical Earth group and Jezero Crater is reduced to 1.3 ± 0.3 and 0.1 pM/yr-cm^3, respectively. Finally, since neither the porosity correction nor the volume correction is

applied here, the reader should note that the ordering from highest to lowest in Figure 7 naturally differs from that of Figure 6.

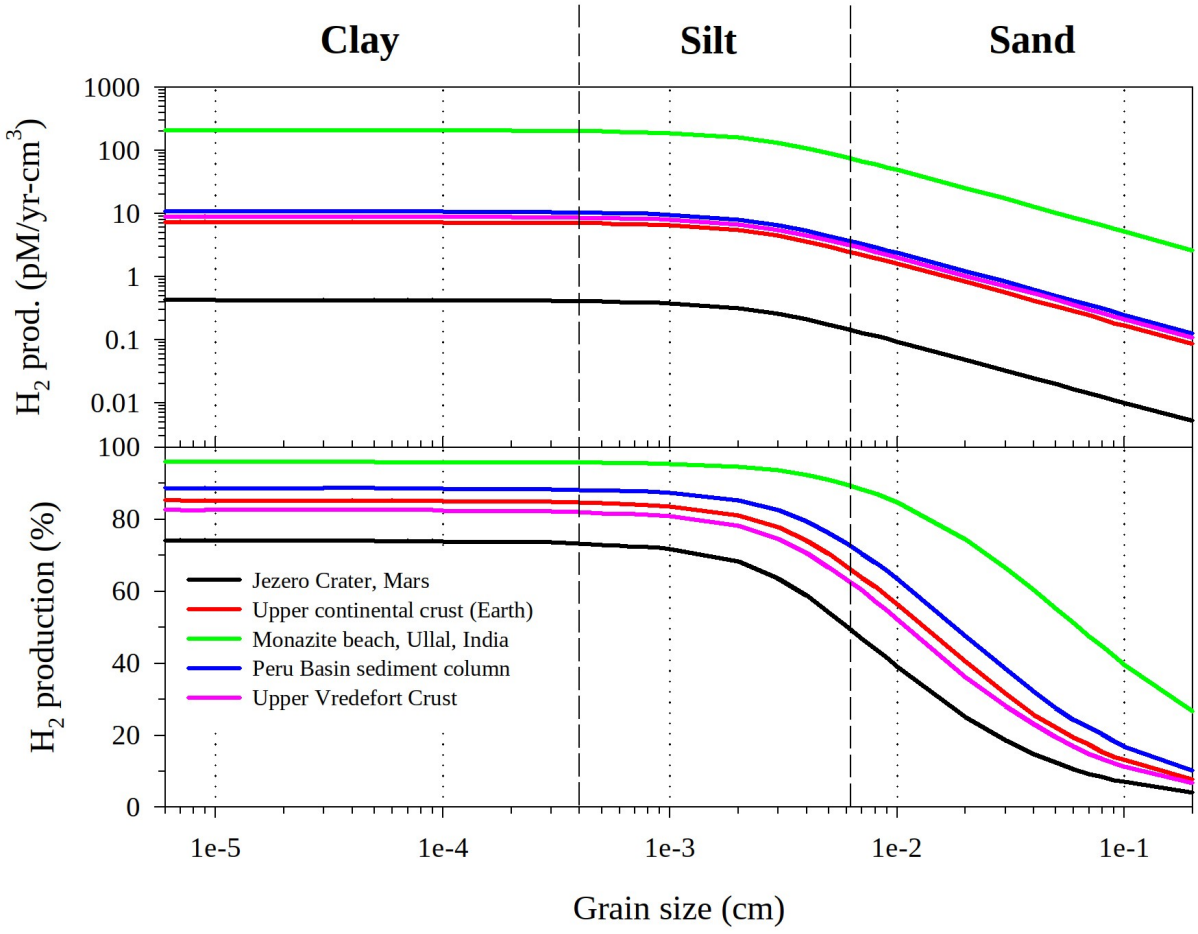


Figure 8. Radiolytic hydrogen production due to **alpha** decay as a function of SiO_2 grain size in a variety of geological formations.

Figure 8 (top) shows H_2 production due to alpha decay in units of pico (p, E-12) moles per [Earth] year-cm^3 as a function of SiO_2 grain radius in cm for a variety of geological formations. With regard to alpha decay only, the output from the MC simulations shows that the monazite beach sand of Ullal, India produces the highest H_2 flux overall, while Jezero Crater on Mars produces the lowest; this finding is consistent across all grain sizes. Furthermore, because of their comparable concentrations of thorium and uranium—which decay largely via alpha emission—the typical Earth group produces similar amounts of H_2 across all grain sizes. Beyond these general observations, Figure 8 is consistent with Figure 5 regarding the attenuation of alpha radiation as compared to beta (Figure 9) and gamma (Figure 10). Figure 8 (bottom) shows H_2 production in terms of percent fraction as a function of SiO_2 grain radius in cm.

When only alpha radiation is considered, our simulations predict that radiolytic hydrogen production would be ~207 ± 2 pM/yr-cm^3 if monazite beach sand were reduced to a grain size in the range of clay. The typical Earth group displays a middle ground of H_2 flux due to alpha decay, with an average of 8.9 ± 1.7 pM/yr-cm^3 in clay. As noted before, this is due to their similar concentrations of thorium and uranium. Jezero Crater is expected to produce a flux that is an order of magnitude below the typical Earth group, with an estimate of 0.42 ± 0.01 pM/yr-cm^3. From the standpoint of alpha decay, our simulations show (in descending order) 95.81 ± 0.04 % (if reduced to clay), 88.5 ± 0.1 %, 85.1 ± 0.2 %, and 82.5 ± 0.2 % for monazite beach sediment, the Peru Basin sediment column, the average of the upper continental crust of the Earth, and Upper Vredefort Crust, respectively, with an average of 85.4 ± 3.0 % for the typical Earth group. This is explained by the ^{232}Th and ^{238}U parameters of Table 2, which are derived from the source thorium and uranium measurements of previous studies. (The result for Jezero Crater is slightly lower at 73.9 ± 0.3 % for the same reason.)

All geological settings studied here attenuate in a predictable manner in silt-sized grains, with estimates of 76.9, 3.2 ± 0.6, and 0.1 pM/yr-cm^3 for monazite beach sand (if appropriately reduced in grain size), the typical Earth group, and Jezero Crater, respectively. Similar to Figure 5 (bottom), in silt the effect of increased grain size is visible on the percent fraction of H_2 production due to alpha decay. This is explained by the tendency of alpha particles to range-out in grain sizes comparable to the characteristic stopping distance of natural radioactive decay. The similar shapes of the curves observed in the typical Earth group are due to their analogous radioactive composition; at the upper bound of silt, the percent contribution from alpha decay is reduced to 67.7 ± 5.0 %. Bookending the typical Earth group are size-adjusted monazite beach sediment and Jezero Crater, which are reduced to 89.6% and 50.1%, respectively.

In grain sizes characteristic of sand, Figure 8 shows that H_2 production due to alpha decay is reduced substantially: At ~0.2 cm, this figure gives estimates of 2.59, 0.11 ± 0.02, and 0.005 pM/yr-cm^3 for monazite beach sand, the typical Earth group, and Jezero Crater, respectively. Similar to Figure 5 (bottom), alpha emissions from natural radioactive decay are further attenuated in sand. At the upper bound (~0.2 cm), alpha emission contributes 26.5%, 8.2 ± 1.8 %, and 4.2% to H_2 production in monazite beach sand, the typical Earth group, and Jezero Crater, respectively. As noted in Figure 5, the upper bound of sand in Figure 8 displays a tapering effect that is consistent with the escape efficiency of alpha particles seen in Figure 2.

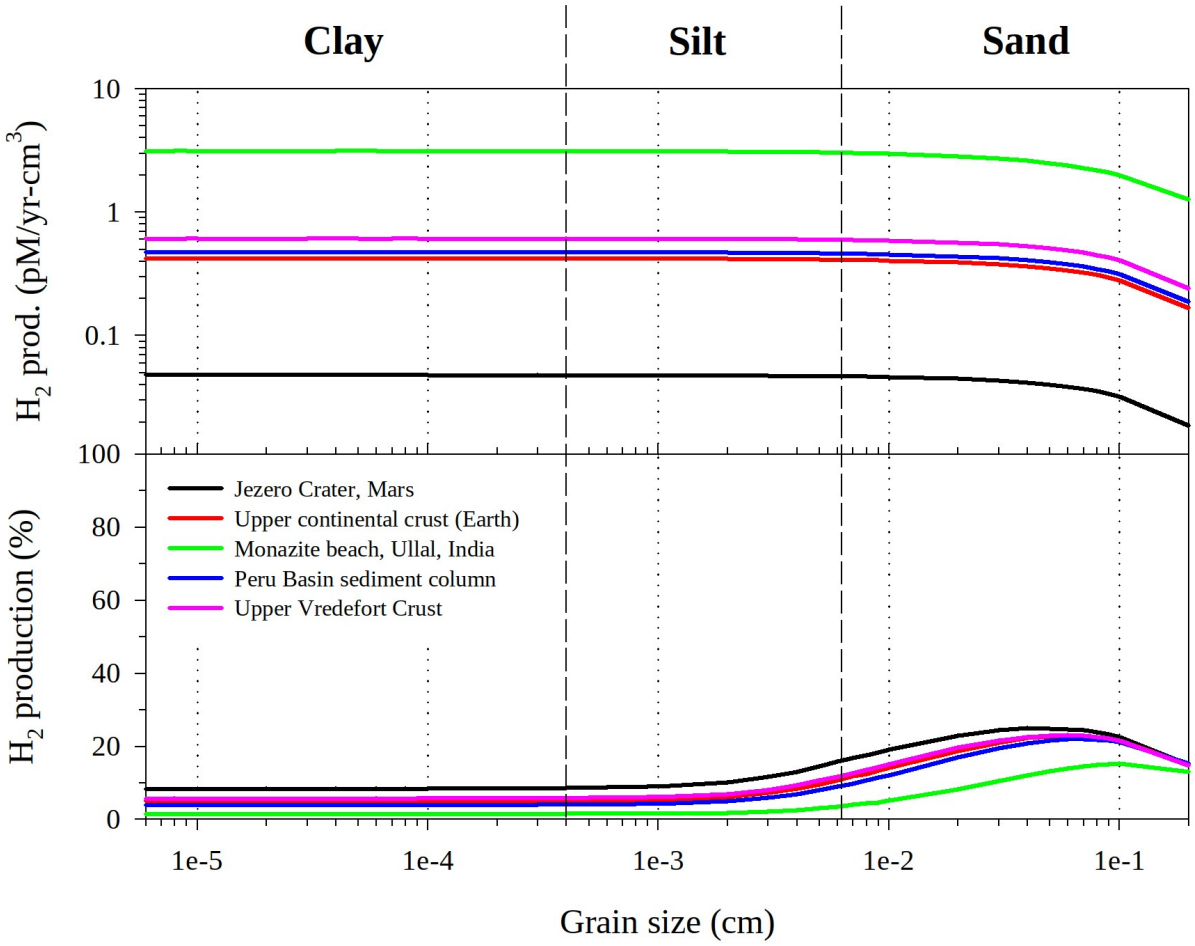


Figure 9. Radiolytic hydrogen production due to **beta** decay as a function of SiO_2 grain size in a variety of geological formations.

Figure 9 (top) shows H_2 production due to beta decay in units of pico (p, E-12) moles per [Earth] year-cm^3 as a function of SiO_2 grain radius in cm for a variety of geological formations. In contrast to Figure 8, where the attenuation of alpha particles is observed in silt, in Figure 9 this same phenomenon occurs in grain sizes that characterize sand. This is explained by the substantially larger stopping distance of beta particles that are routinely emitted via natural radioactive decay (~0.05 cm). Similar to Figure 8, this figure also shows that—across all grain sizes—the monazite beach sand of Ullal, India produces the most H_2 overall, a finding that is one order of magnitude above the typical Earth group. Figure 9 (bottom) shows H_2 production in terms of percent fraction as a function of SiO_2 grain radius in cm. Here a local maximum in sand is observed for all geological units.

If monazite beach sand were reduced to a grain size in the range of clay, our simulations predict that radiolytic hydrogen production would be approximately constant at 3.122 ± 0.002 pM/yr-cm^3. In clay the typical Earth group displays an H_2 flux due to beta decay that is one order of magnitude smaller: 0.5 ± 0.1 pM/yr-cm^3. Jezero Crater on Mars is expected to produce a flux that is an order of magnitude below the typical Earth group, with an estimate of 0.04776 ± 0.00003 pM/yr-cm^3. In descending order, our simulations show percent fraction contributions

due to beta decay of 8.37 ± 0.08 %, 4.84 ± 0.9 %, and 1.45 ± 0.01 % for Jezero Crater, the typical Earth group, and monazite beach sand (in the form of clay), respectively. Similar to Figure 8, these results are explained by the ^{40}K parameters of Table 2, where potassium decays the most frequently via beta emission.

Figure 9 shows that monazite beach sand, if reduced to grain sizes characteristic of silt, is predicted to produce an H_2 flux due to beta emission that is only slightly diminished compared to that in clay, or 3.0 pM/yr-cm^3 at the upper bound. What is more, the typical Earth group shows almost no variation both qualitatively and quantitatively (at ~0.006 cm: 0.5 ± 0.1 pM/yr-cm^3). This is also observed in the case of Jezero Crater, or 0.04685 pM/yr-cm^3 at the upper bound of silt. Examining Figure 9 (bottom), if monazite beach sand were reduced to silt, the percent contribution due to beta decay would increase marginally to 3.5% at the upper bound. Furthermore, Jezero Crater and the typical Earth group also increase to 15.8% and 10.5 ± 1.4 %, respectively. Comparing these results to Figure 8 (bottom), we can understand this phenomenon in terms of the tendency of alpha particles to range-out in silt (i.e., beta compensates proportionally).

In grain sizes characteristic of sand, where beta particles from natural radioactive decay have the tendency to range-out, H_2 production is reduced. Specifically, at the upper bound (~0.2 cm), Figure 9 (top) gives estimates of 1.27, 0.20 ± 0.04, and 0.02 pM/yr-cm^3 for monazite beach sand, the typical Earth group, and Jezero Crater, respectively. Beta emissions are substantially attenuated in sand where the characteristic range of these particles (~0.05 cm) is comparable to the grain size. That is, beta particles range-out in sand in much the same way as alpha particles in silt. Moreover, it can be seen from Figure 9 that the peak contribution from beta emission occurs at about 0.04, 0.06, and 0.1 cm for Jezero Crater, the typical Earth group, and monazite beach sand, respectively.

Figure 10 shows H_2 production due to gamma decay in units of pico (p, E-12) moles per [Earth] year-cm^3 as a function of SiO_2 grain radius in cm for a variety of geological formations. In contrast to alpha and beta emission, no attenuation is observed in radiolytic hydrogen production as a function of grain size. This is explained by 1) the differing physics of photon interaction with matter, and 2) the large attenuation length (~3.2 cm) characteristic of gamma decay in a natural setting. Similar to Figure 9 (bottom), this figure shows that Jezero Crater produces the most H_2 across all grain sizes due to gamma decay, while monazite beach sand produces the least, with the typical Earth group presenting a middle ground. These results are sensible given the ^{40}K parameters of Table 2, which suggest the frequent emission of a residual gamma ray as radioactive potassium decays to ^{40}Ar.

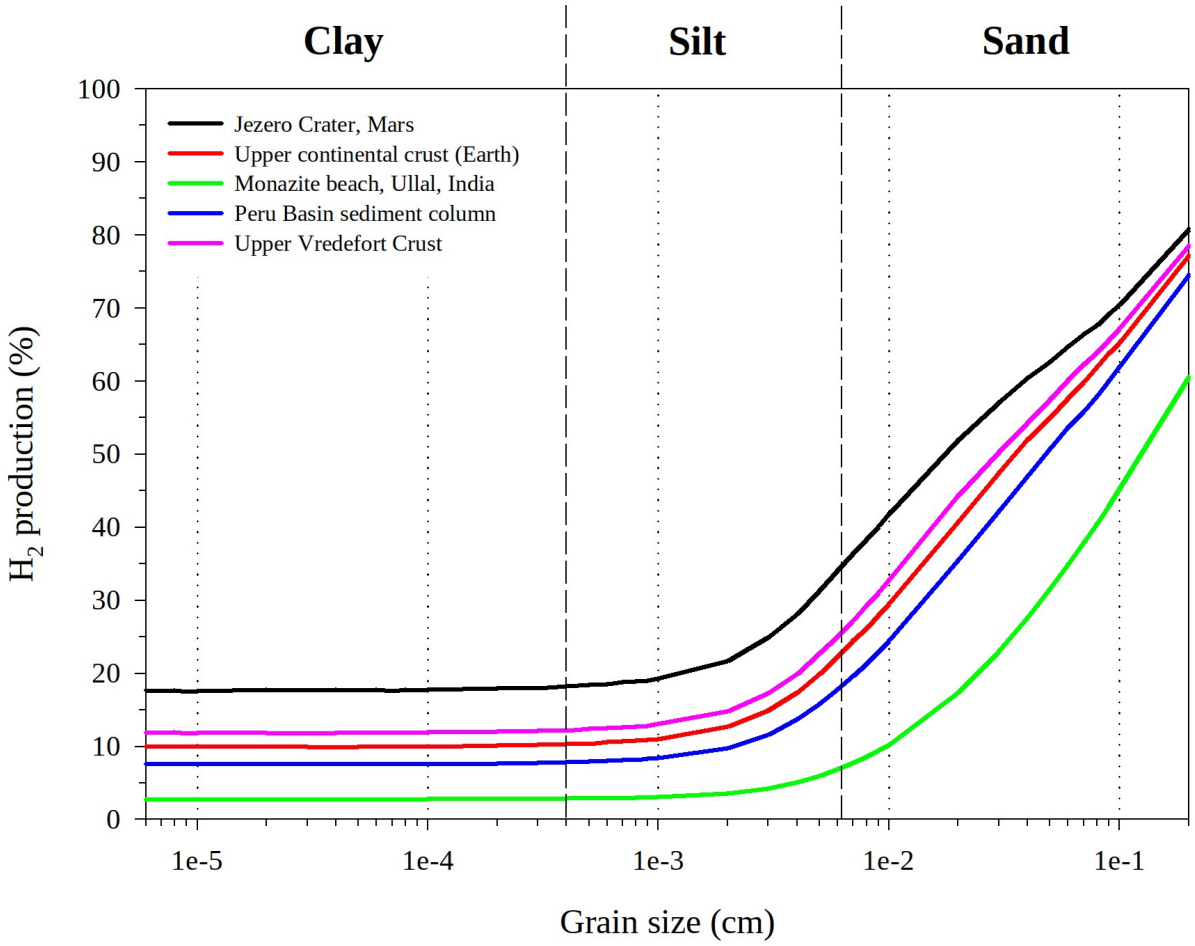


Figure 10. Radiolytic hydrogen production due to gamma decay as a function of SiO_2 grain size in a variety of geological formations.

Gamma rays are photons that lack charge and mass. Consequently they are not subject to electromagnetic slowing as in the case of alpha and beta particles. Thus, the H_2 contribution of gamma rays is constant where the grain size is much less that the characteristic attenuation length found in natural radioactive decay. Our simulations confirm this phenomenon with a summary in Table 3.

Table 3. Average H_2 production in units of pM/yr-cm^3 due to gamma decay for a variety of geological settings predicted using the parameters given in Table 2.

	Jezero Crater, Mars	Upper continental crust (Earth)	Monazite beach sediment, Ullal, India	Peru Basin sediment column	Upper Vredefort Crust
Average	0.10122	0.8509	5.928	0.9185	1.278

Standard Deviation	0.00004	0.0004	0.002	0.0004	0.001

In clay (0.06 - 4 μm), Figure 10 shows percent fraction contributions due to gamma decay of 17.7 ± 0.2 %, 9.8 ± 2.2 %, and 2.74 ± 0.03 % for Jezero Crater, the typical Earth group, and monazite beach sand (size-reduced), respectively, in descending order. As noted in Figure 9 (bottom), the sequencing observed here is attributed to the relative radioactivity of these geological formations.

In silt (5 - 60 μm), this figure shows that Jezero Crater, the typical Earth group, and monazite beach sand (reduced in size to silt) increase to 34.1%, 21.8 ± 3.6 %, and 6.9%, respectively. As noted previously, this is a further consequence of the tendency of alpha particles to range-out in silt, where beta (Figure 9, bottom) and gamma (Figure 10) compensate proportionally.

In sand (70 - 2,000 μm), alpha and beta particles are shown to have a diminished effect on the percent contribution to H_2 production. At this point gamma emission dominates radiolytic hydrogen production to the extent that Jezero Crater, the typical Earth group, and monazite beach sand contribute 80.9%, 76.8 ± 2.0 %, and 60.6%, respectively, at the upper bound. Gamma rays characteristic of natural radioactive decay are expected to attenuate in grain sizes of between one and two orders of magnitude beyond those of sand.

4. Discussion and Conclusions

This study has developed and validated a Monte Carlo method that simulates the physics of mineral radiation in order to predict the production of H_2 as a function of mineral grain size and radioisotope composition. The results given here confirm that grain size is a major control on overall radioactivity, and consequently, on radiolytic H_2 yield. The dominant mode of decay (i.e., as controlled by the radioisotope composition) also tends to influence the degree to which H_2 flux is attenuated as a function of grain size; materials whose radioactivity is dominated by their potassium content will show a less severe attenuation of H_2 flux with increasing grain size since ^{40}K radiation is dominated by beta rather than alpha emissions. When our method is applied to a generic test case, the standard geological classification of grain sizes seems to suggest that clay can produce up to an order of magnitude more H_2 per unit time than sand. Furthermore, we have used the physics encoded in our simulation method to confirm that alpha particles range-out in silt, while beta particles range-out in grain sizes characteristic of sand. Additionally, all gamma rays, by virtue of their attenuation length, were found to escape to the surrounding water layer in our simulations, with the result that gamma radiation dominates H_2 production for grain sizes larger than sand. Consequently, we do not expect gamma radiation to attenuate until grain sizes exceed those of sand by at least one order of magnitude.

We have applied our numerical method to a variety of interesting natural systems as a means of exploring the magnitude of porewater radiolysis. This exploration was conducted using compositional data from real geological units in order to demonstrate the dependence of natural radionuclide concentration and bulk porosity on radiolytic hydrogen flux. A survey of our simulation results seems to suggest that H_2 production in these geological units is modulated by

771 alpha decay in rock/sediment grain sizes characteristic of clay and silt, while beta and gamma
772 emissions take over as a secondary control in sand-sized grains.

773 These results were obtained for spherical grains. In real rocks and sediments, grains of a
774 size likely to attenuate alpha radiation considerably (e.g., sand) are likely to be fairly spherical
775 and equant, whereas highly non-spherical grains (e.g., platy clay crystals) are likely to be small
776 and thus minimally attenuating. It follows that our general results may be fairly realistic for
777 complex geological materials. Nevertheless, our Monte Carlo method can be readily adapted for
778 materials with constituent grains of arbitrary size and shape, of any composition, on any
779 planetary body. As a consequence, it should now be possible to estimate more accurately how
780 radiolytic hydrogen might contribute to the habitability of microbial life in porous materials on
781 Earth, Mars, and beyond.

782

783 **Acknowledgments and Data**

784 The authors greatly appreciate the helpful discussions with Eric Benton at Oklahoma
785 State University and Regina DeWitt at East Carolina University. S.M. also thanks Barry B.
786 McMahon for helpful discussions about the geometry in Supplementary Information S2.

787

788 **References**

789 Aitken, M. J. (1985). *Thermoluminescence Dating*. Orlando: Academic Press.

790 Aquilina, L., de Dreuzy, J. R., Bour, O., & Davy, P. (2004). Porosity and fluid velocities in the
791 upper continental crust (2 to 4 km) inferred from injection tests at the Soultz-sous-Forêts
792 geothermal site. *Geochimica et Cosmochimica Acta*, *68*(11), 2405-2415.

793 Bethe, H. (1930). Zur theorie des durchgangs schneller korpuskularstrahlen durch
794 materie. *Annalen der Physik*, *397*(3), 325-400.

795 Bethe, H., & Heitler, W. (1934). On the stopping of fast particles and on the creation of positive
796 electrons. *Proceedings of the Royal Society of London. Series A, Containing Papers of a*
797 *Mathematical and Physical Character*, *146*(856), 83-112.

798 Blair, C. C., D'Hondt, S., Spivack, A. J., & Kingsley, R. H. (2007). Radiolytic hydrogen and
799 microbial respiration in subsurface sediments. *Astrobiology*, *7*(6), 951-970.

800 Brookhaven National Laboratory (2021). Interactive Chart of Nuclides (2021),
801 http://www.nndc.bnl.gov/nudat2

802 Bouquet, A., Glein, C. R., Wyrick, D., & Waite, J. H. (2017). Alternative energy: production of
803 H2 by radiolysis of water in the rocky cores of icy bodies. *The Astrophysical Journal*
804 *Letters*, *840*(1), L8.

805 Chapelle, F. H., O'Neill, K., Bradley, P. M., Methé, B. A., Ciufo, S. A., Knobel, L. L., & Lovley,
806 D. R. (2002). A hydrogen-based subsurface microbial community dominated by
807 methanogens. *Nature*, *415*(6869), 312-315.

Clifford, S. M., Lasue, J., Heggy, E., Boisson, J., McGovern, P., & Max, M. D. (2010). Depth of the Martian cryosphere: Revised estimates and implications for the existence and detection of subpermafrost groundwater. *Journal of Geophysical Research: Planets*, *115*(E7).

Dzaugis, M. E., Spivack, A. J., Dunlea, A. G., Murray, R. W., & D'Hondt, S. (2016). Radiolytic hydrogen production in the subseafloor basaltic aquifer. *Frontiers in microbiology*, *7*, 76.

Dzaugis, M., Spivack, A. J., & D'Hondt, S. (2018). Radiolytic H2 production in martian environments. *Astrobiology*, *18*(9), 1137-1146.

Einstein, A. (1905). Über einen die Erzeugung und Verwandlung des Lichtes betreffenden heuristischen Gesichtspunkt Annalen der Physik 17, 132.

Fermi, E. (1940). The ionization loss of energy in gases and in condensed materials. *Physical Review*, *57*(6), 485.

Fowler, A. C., & Yang, X. S. (1998). Fast and slow compaction in sedimentary basins. *SIAM Journal on Applied Mathematics*, *59*(1), 365-385.

Freund, F., Dickinson, J. T., & Cash, M. (2002). Hydrogen in rocks: an energy source for deep microbial communities. *Astrobiology*, *2*(1), 83-92.

Gleeson, T., Befus, K. M., Jasechko, S., Luijendijk, E., & Cardenas, M. B. (2016). The global volume and distribution of modern groundwater. *Nature Geoscience*, *9*(2), 161-167.

Gould, R. J., & Schréder, G. P. (1967). Pair production in photon-photon collisions. *Physical Review*, *155*(5), 1404.

Hofmann, B.A. (1992). Isolated reduction phenomena in red beds: a result of porewater radiolysis. In Y.K. Kharaka, and A.S. Maest (Eds.), *Water–Rock Interaction* (pp 503–506). Rotterdam: A.A. Balkema.

Klein, O., & Nishina, Y. (1929). Über die Streuung von Strahlung durch freie Elektronen nach der neuen relativistischen Quantendynamik von Dirac. *Zeitschrift für Physik*, *52*(11), 853-868.

Kral, T. A., Brink, K. M., Miller, S. L., & McKay, C. P. (1998). Hydrogen consumption by methanogens on the early Earth. *Origins of Life and Evolution of the Biosphere*, *28*(3), 311-319.

Krumholz, L. R., McKinley, J. P., Ulrich, G. A., & Suflita, J. M. (1997). Confined subsurface microbial communities in Cretaceous rock. *Nature*, *386*(6620), 64-66.

Lefticariu, L., Pratt, L. A., LaVerne, J. A., & Schimmelmann, A. (2010). Anoxic pyrite oxidation by water radiolysis products—a potential source of biosustaining energy. *Earth and Planetary Science Letters*, *292*(1-2), 57-67.

Lin, L. H., Hall, J., Lippmann-Pipke, J., Ward, J. A., Sherwood Lollar, B., DeFlaun, M., et al. (2005). Radiolytic H2 in continental crust: nuclear power for deep subsurface microbial communities. *Geochemistry, Geophysics, Geosystems*, *6*(7).

McCollom, T. M. (1999). Methanogenesis as a potential source of chemical energy for primary biomass production by autotrophic organisms in hydrothermal systems on Europa. *Journal of Geophysical Research: Planets*, *104*(E12), 30729-30742.

McMahon, S., & Parnell, J. (2014). Weighing the deep continental biosphere. *FEMS Microbiology Ecology*, *87*(1), 113-120.

McMahon, S., Parnell, J., & Blamey, N. J. (2016). Evidence for seismogenic hydrogen gas, a potential microbial energy source on Earth and Mars. *Astrobiology*, *16*(9), 690-702.

National Institute of Standards and Technology (2021a), Stopping-power and range tables for helium ions, physics.nist.gov/PhysRefData/Star/Text/ASTAR.html.

National Institute of Standards and Technology (2021b), Stopping-power and range tables for electrons, physics.nist.gov/PhysRefData/Star/Text/ESTAR.html.

Nixon, S., Cousins, C. R., & Cockell, C. (2013). Plausible microbial metabolisms on Mars. *Astronomy & Geophysics*, 54, 1.13-1.16.

Lane, N., & Martin, W. F. (2012). The origin of membrane bioenergetics. *Cell*, *151*(7), 1406-1416.

Preiner, M., Igarashi, K., Muchowska, K. B., Yu, M., Varma, S. J., Kleinermanns, K., et al. (2020). A hydrogen-dependent geochemical analogue of primordial carbon and energy metabolism. *Nature ecology & evolution*, *4*(4), 534-542.

Radhakrishna, A.P., Somashekarappa, H.M., Narayana, Y., & Siddappa, K.A. (1993). New natural background radiation area on the southwest coast of India. *Health Physics 65*(4), 390–395

Schulte, M., Blake, D., Hoehler, T., & McCollom, T. (2006). Serpentinization and its implications for life on the early Earth and Mars. *Astrobiology*, *6*(2), 364-376.

Sleep, N. H., Bird, D. K., & Pope, E. C. (2011). Serpentinite and the dawn of life. *Philosophical Transactions of the Royal Society B: Biological Sciences*, *366*(1580), 2857-2869.

Smetannikov, A. F. (2011). Hydrogen generation during the radiolysis of crystallization water in carnallite and possible consequences of this process. *Geochemistry International*, *49*(9), 916-924. [Sonzogni and Shu, 2020] Sonzogni, A. and Shu, B. (2020), Nudat 2, www.nndc.bnl.gov/nudat2/.

Spinks, J. W. T., & Woods, R. J. (1990). *An Introduction to Radiation Chemistry*. New York: Wiley.

Stevens, T. O., & McKinley, J. P. (1995). Lithoautotrophic microbial ecosystems in deep basalt aquifers. *Science*, *270*(5235), 450-455.

Tarnas, J. D., Mustard, J. F., Sherwood Lollar, B., Bramble, M. S., Cannon, K. M., Palumbo, A. M., & Plesa, A. C. (2018). Radiolytic H2 production on Noachian Mars: implications for habitability and atmospheric warming. *Earth and Planetary Science Letters*, *502*, 133-145.

Tarnas, J.D., Mustard, J.F., Sherwood Lollar, B., Stamenković, V., Cannon, K.M., Lorand, J.P., et al., 2021. Earth-like Habitable Environments in the Subsurface of Mars. *Astrobiology*, *21*(6), 741–756.

Taylor, J.R. (1996). *An Introduction to Error Analysis: The Study of Uncertainties in Physical Measurements*, 2nd Edition., Sausalito, CA: University Science Books.

Waite, J. H., Glein, C. R., Perryman, R. S., Teolis, B. D., Magee, B. A., Miller, G., et al. (2017). Cassini finds molecular hydrogen in the Enceladus plume: evidence for hydrothermal processes. *Science*, *356*(6334), 155-159.

Weaver, B. A., & Westphal, A. J. (2002). Energy loss of relativistic heavy ions in matter. *Nuclear Instruments and Methods in Physics Research Section B: Beam Interactions with Materials and Atoms*, *187*(3), 285-301.

Webster, C. R., Mahaffy, P. R., Atreya, S. K., Flesch, G. J., Mischna, M. A., Meslin, P. Y., ... & Lemmon, M. T. (2015). Mars methane detection and variability at Gale crater. *Science*, *347*(6220), 415-417.

Wentworth, C. K. (1922). A scale of grade and class terms for clastic sediments. *The Journal of Geology*, *30*(5), 377-392.

Geochemistry, Geophysics, Geosystems

Supporting Information for

The Effect of Grain Size on Porewater Radiolysis

J. DeWitt[1], S. McMahon[2,3], and J. Parnell[4]

[1] Department of Physics, East Carolina University,
Howell Science Complex, 10th Street, Greenville NC 27858, US

[2] School of Physics and Astronomy, University of Edinburgh,
James Clerk Maxwell Building, Peter Guthrie Tait Road, Edinburgh EH9 3FD, UK

[3] School of Geosciences, University of Edinburgh, Grant Institute, Edinburgh EH9 3FE, UK

[4] School of Geosciences, University of Aberdeen, Meston Building, King's College, Aberdeen AB24 3UE

Contents of this file

Text S1 and S2
Figures S1–S3

Introduction

- This supporting information contains the algorithmic foundation of the Fortran code used in the model (Text S1) and a derivation of Equation 5 (alpha particle escape efficiency from spherical grains) used in the paper (Text S2, supported by Figures S1–S3).

Text S1.

```
PROGRAM Alpha_escape
```

```
  USE Shared
  IMPLICIT NONE
  CALL INIT_RANDOM_SEED()
  PRINT *, " "
  OPEN(Alpha_escape_txt, file='Alpha_escape.txt',
access='sequential', status='unknown', action='write',
asynchronous='yes')
  WRITE(Alpha_escape_txt, '(a9, 3a21)') "r (μm)", "n_alpha",
"E_g", "%diff" !columns
  complete = 5
  radius = MICRON !initialize radius
  ALLOCATE(percent_diff(INT(MAX_RADIUS / MICRON)))
  many_radii: DO
      IF (INT((radius / MAX_RADIUS) * 100.0_dp) == complete)
THEN !keep user apprised of progress
      WRITE(6, '(i5, a1)') complete, "%"
      complete = complete + 5 !next 5% checkpoint
      END IF
      n_alpha = 0 !initialize sum for averaging this radius
      many_alphas: DO number = 1, NUMBER_MAX
      CALL RANDOM_NUMBER(random)
      r_1 = radius * CBRT1(random) !select a random DECAY point
along this radius
      CALL RANDOM_NUMBER(random)
      theta_1 = 2.0_dp * PI * random !select a random azimuthal
DECAY angle
      CALL RANDOM_NUMBER(random)
      IF (radius < S / CM_TO_UM * 1.5_dp) THEN !select a random
polar DECAY angle
      phi_1 = ACOS(2.0_dp * random - 1.0_dp)
      ELSE
      phi_1 = 2.0_dp * PI * random
      END IF
      x_1 = r_1 * COS(theta_1) * SIN(phi_1) !x-coordinate DECAY
      y_1 = r_1 * SIN(theta_1) * SIN(phi_1) !y-coordinate DECAY
      z_1 = r_1 * COS(phi_1) !z-coordinate DECAY
      CALL RANDOM_NUMBER(random)
      theta_2 = 2.0_dp * PI * random !select a random azimuthal
EXIT angle
      CALL RANDOM_NUMBER(random)
      IF (radius < S / CM_TO_UM * 1.4_dp) THEN !select a random
polar EXIT angle
      phi_2 = ACOS(2.0_dp * random - 1.0_dp)
      ELSE
      phi_2 = 2.0_dp * PI * random
      END IF
      r_2 = 0.0_dp !my EXIT vector, also at the origin, but add
tip-to-tail later
      1 x_2 = r_2 * COS(theta_1 + theta_2) * SIN(phi_1 + phi_2)
      y_2 = r_2 * SIN(theta_1 + theta_2) * SIN(phi_1 + phi_2)
      z_2 = r_2 * COS(phi_1 + phi_2)
      x_3 = x_1 + x_2 !add x-components
```

```
      y_3 = y_1 + y_2 !add y-components
      z_3 = z_1 + z_2 !add z-components
      r_3 = SQRT(x_3**2 + y_3**2 + z_3**2) !find resultant vector,
should be the EXIT point on my sphere
      IF (r_3 > radius) THEN
      depth = r_2 !mission accomplished, actual depth of SiO2 to
be traversed before escaping from the SiO2 grain
      ELSE !extend DEPTH vector and repeat
      r_2 = r_2 + DX !looking for an r_3 that looks like the
radius of my sphere
      GO TO 1 !try again
      END IF
      x = 0.0_dp !start at the beginning
      E_i = 4.92991712862015_dp !MeV
      stopping_power_alpha: DO
      IF (dEdx_alpha(E_i) < 0.0_dp) EXIT !check for good stopping
power
      E_f = E_i - (dEdx_alpha(E_i) * DENSITY * DX) !kinetic energy
decreases in MeV while accounting for the density of the absorber
      IF (E_f < 0.0_dp) EXIT !check for good final energy
      IF (x > depth .AND. E_f > 0.0_dp) THEN !ALPHA has escaped
the SiO2 grain
            n_alpha = n_alpha + 1
            EXIT !out-of-bounds, nothing more to do
      END IF
      E_i = E_f !pass for next iteration
      x = x + DX !advance in cm
      END DO stopping_power_alpha
      END DO many_alphas
      theta = 2.0_dp * radius * CM_TO_UM !grain size is diameter
in µm
      E_g = (3.0_dp * S) / (2.0_dp * theta) - (S * S * S) /
(2.0_dp * theta * theta * theta) !McMahon
      percent_diff(NINT(radius * CM_TO_UM)) =
ABS((FLOAT(n_alpha) / FLOAT(NUMBER_MAX)) - E_g) * 100.0_dp
      WRITE(Alpha_escape_txt, '(i8, 3f21.15)') NINT(radius *
CM_TO_UM), (FLOAT(n_alpha) / FLOAT(NUMBER_MAX)) * 100.0_dp,
      &
      E_g * 100.0_dp, percent_diff(NINT(radius * CM_TO_UM))
      IF (radius > MAX_RADIUS) EXIT !cm
      radius = radius + MICRON
  END DO many_radii
  PRINT *, " "
  PRINT *, "Average percent difference:",
SUM(percent_diff(10:SIZE(percent_diff))) / SIZE(percent_diff)
  DEALLOCATE(percent_diff)
  CLOSE(Alpha_escape_txt)
  PRINT *, " "
END PROGRAM Alpha_escape
```

Text S2.

For particles with stopping distance *s* emitted in random directions and originating at random points inside a spherical grain of diameter Θ, the proportion of these particles that exit the grain rather than terminating within it can be estimated as follows.

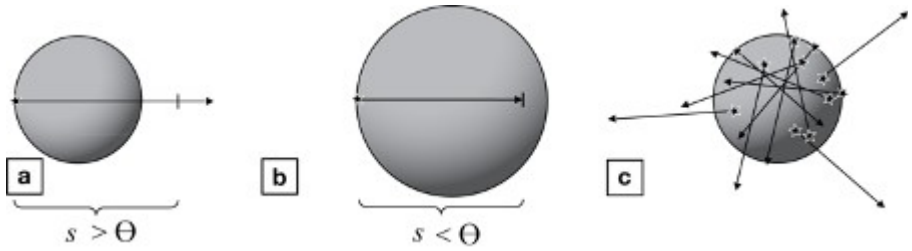


Figure S1. Alpha particle emission by sediment grains. (a) When the stopping distance exceeds the grain diameter, all alpha particles escape. (b) When the grain diameter exceeds the stopping distance, some alpha particles are trapped. (c) Alpha particles are emitted throughout each grain and travel in random directions.

If the grain diameter is less than the stopping distance, all particles emitted from anywhere in the grain will be able to escape, since the longest distance that any particle has to travel before escaping is Θ (**Figure S1a**). However, if Θ > *s*, then some of the particles (e.g., those emitted inwards from near the grain edge) will be stopped (**Figure S1b**) while others will escape (e.g., those emitted outwards from the same point).

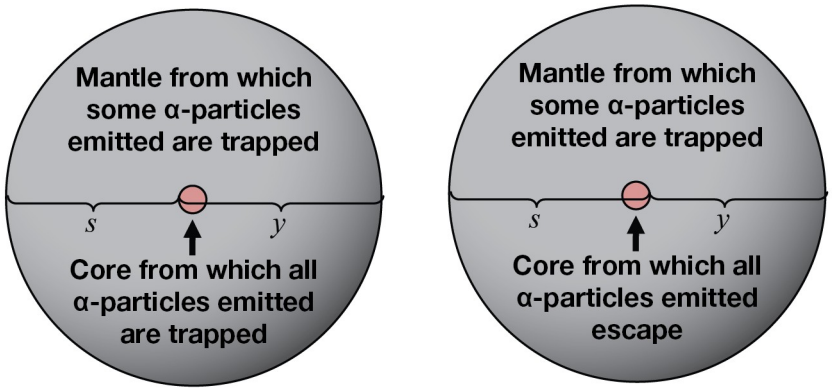


Figure S2. (Left) When the stopping distance of an alpha particle is less than the radius of the grain (i.e., $y > s$; $\Theta > 2s$), there is a "core" region such that particles emitted from this core cannot escape from the grain. Of those particles generated in the rest of the grain (the "mantle"), some escape and others are trapped, depending on their trajectories. **(Right)** When the stopping distance of the alpha particle is greater than the radius of the grain (i.e., $y < s$; $\Theta > 2s$), there is a core region from which all particles escape, and a mantle from which some are trapped.

Referring to **Figure S2**, let y be Θ – *s*. Furthermore, let E_g be the fraction of particles emitted in the grain that escapes, which is 1 – T_g, the fraction trapped. The case where $y > s$ (i.e., $\Theta > 2s$) is considered first. In this case, the radius of the grain is longer than the stopping distance of the particle. There is a core region of the grain from which all particles emitted are trapped (**Figure S2, left**).

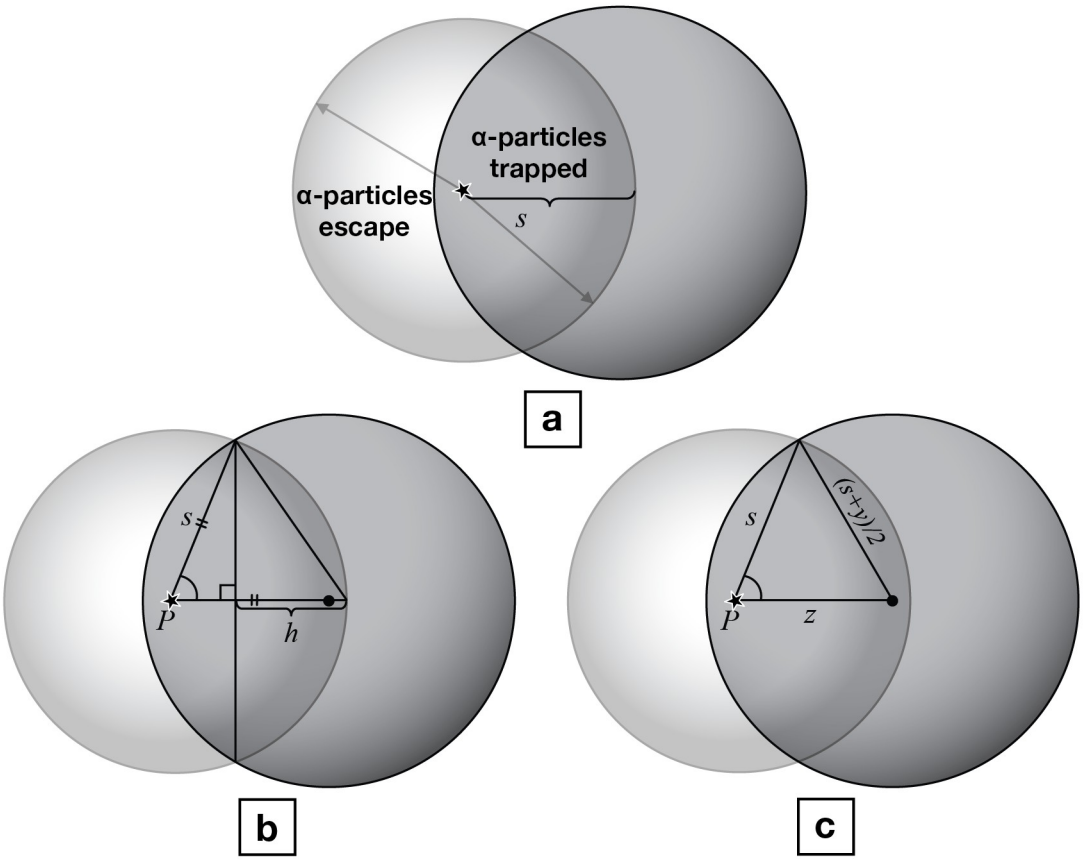


Figure S3. Alpha particles are emitted from a point (star) in a spherical grain (dark grey). **(a)** The possible trajectories of the alpha particles are indicated by the light grey sphere, whose radius is the stopping distance. Part of the surface of this sphere lies inside the grain; the area of this surface (i.e., a spherical cap) divided by the total area of the sphere gives the proportion of particles emitted from this point that would be trapped within the grain. Panels **(b)** and **(c)** show constructions used in the derivation.

This core region has diameter $y - s$ and volume V_c. The remainder of the grain is a mantle with volume V_m. Of those particles emitted inside this mantle, a certain proportion escape, and a certain proportion T_m are trapped because they have to travel a distance s into the grain (**Figure S3**). If ρ is the number of particles emitted per unit volume, then

$$T_g = \frac{\rho V_c + \rho V_m T_m}{\rho V_g}, \qquad \text{(S1)}$$

where ρ naturally cancels.

The mantle is regarded as the sum of concentric spherical shells of radius z and infinitesimal thickness dz. Each shell emits a different number of particles, a fraction of which are trapped. This fraction $T_{P,z}$ is equal to the number of particles trapped divided by the number emitted from any individual point P in the shell, i.e., at distance z from the centre of the grain. $T_{P,z}$ is equal to the proportion of the surface area of a sphere of diameter s, centred at P, that lies inside the grain. If the surface area of the sphere is $4\pi s^2$, then a partial area trapped within the grain (a spherical cap) is given by

$2\pi sh$, where h is the distance between the outer edge of the sphere and the plane where it intersects the grain (the trace of this plane appears as a vertical line in **Figure S3b**). The distance h was found using the constructions shown in **Figure S3b-c**.

The trigonometry in **Figure S3b** gives

$$\cos(P)=\frac{s-h}{s} \tag{S2}$$

Applying the law of cosines to **Figure S3c** gives

$$\cos(P)=\frac{s^2+z^2-\frac{(s+y)^2}{4}}{2sz} \tag{S3}$$

Equating Equations S2 and S3 gives

$$h=s-\frac{s^2+z^2-\frac{(s+y)^2}{4}}{2z} \tag{S4}$$

Normalizing Equation S4 appropriately gives

$$T_{P,z}=\frac{2\pi s}{4\pi s^2}\left(s-\frac{s^2+z^2-\frac{(s+y)^2}{4}}{2z}\right) \tag{S5}$$

Simplifying Equation S5 gives a more manageable polynomial:

$$T_{P,z}=\frac{1}{2}+\frac{(s+y)^2-4s^2}{16s}z^{-1}-\frac{1}{4s}z \tag{S6}$$

To find V_mT_m, the volumes of the infinitesimal shells of thickness dz that make up the mantle were multiplied by $T_{P,z}$ (the fraction of trapped particles from each shell) and integrated over the range of z in the mantle. The volume of each shell is naturally equal to $4\pi z^2dz$. The limits of integration are $(y - s)/2$ at the inner edge of the mantle and $(s + y)/2$ at the surface of the grain. Therefore,

$$V_mT_m=4\pi\int_{z=\frac{y-s}{2}}^{z=\frac{s+y}{2}}z^2\left(\frac{1}{2}+\frac{(s+y)^2-4s^2}{16s}z^{-1}-\frac{1}{4s}z\right)dz \tag{S7}$$

Integrating as usual gives

$$V_mT_m=4\pi\left[\frac{(s+y)^2-4s^2}{32s}z^2+\frac{1}{6}z^3-\frac{1}{16s}z^4\right]_{z=\frac{y-s}{2}}^{z=\frac{s+y}{2}} \tag{S8}$$

Applying the limits of integration and simplifying gives $V_m T_m = \frac{\pi}{12}$¿). Recalling Equation S1 and substituting the expressions for V_g , V_c and $V_m T_m$ gives

$$T_g = \frac{\left(\frac{(y-s)}{2}\right)^3 + \frac{1}{16}\left(2s^3 - 6s^2 y + 9 s y^2\right)}{\left(\frac{(s+y)}{2}\right)^3} \quad \text{(S9)}$$

After some simplification we have

$$T_g = \frac{y^2(3s+2y)}{2(s+y)^3} \quad \text{(S10)}$$

Since $s + y$ is equal to the grain diameter Θ, we arrive at the result:

$$T_g = \frac{s^3}{2\Theta^3} - \frac{3s}{2\Theta} + 1 \quad \text{(S11)}$$

If Θ > s, then $E_g = 1 - T_g$, or

$$E_g(\theta) = \frac{3s}{2\Theta} - \frac{s^3}{2\Theta^3} \quad \text{(S12)}$$

Analytically, the proportion of escaped alpha particles is given by Equation S12 as a function of grain size Θ for a given stopping distance s. In the case where $y < s$, or Θ > $2s$, there is a core region from which all particles escape (**Figure S2, right**); a derivation analogous to that above also produces Equation S12, which in any case provides a way to validate the geometry of the Monte Carlo method.